Cell Reports

Article

NAD depletion mediates cytotoxicity in human neurons with autophagy deficiency

Graphical abstract

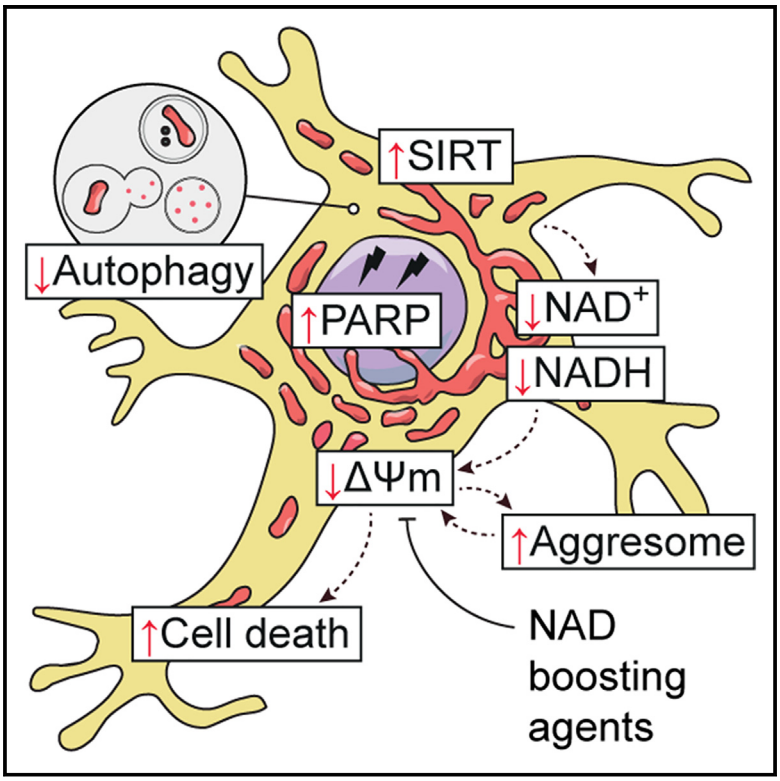

Authors

Congxin Sun, Elena Seranova, Malkiel A. Cohen, ..., Rudolf Jaenisch, Viktor I. Korolchuk, Sovan Sarkar

Correspondence

viktor.korolchuk@newcastle.ac.uk (V.I.K.), s.sarkar@bham.ac.uk (S.S.)

In brief

Sun et al. establish human neurons with loss of autophagy where depletion of nicotinamide adenine dinucleotide (NAD) mediates cytotoxicity. Boosting NAD levels improves the viability of autophagy-deficient human neurons by restoring mitochondrial bioenergetics and proteostasis, providing insights for therapeutic interventions in neurodegenerative diseases associated with autophagy dysfunction.

Highlights

- Loss of autophagy in hESCs and neurons causes a metabolic defect and cell death
- Depletion of NAD triggers cell death via mitochondrial depolarization
- NAD exhaustion occurs due to hyperactivation of NAD-consuming enzymes
- NAD-boosting agents rescue the viability of autophagy-deficient human neurons

Sun et al., 2023, Cell Reports *42*, 112372
May 30, 2023
https://doi.org/10.1016/j.celrep.2023.112372

CellPress

Cell Reports

CellPress
OPEN ACCESS

Article

NAD depletion mediates cytotoxicity in human neurons with autophagy deficiency

Congxin Sun,[1,27] Elena Seranova,[1,22,27] Malkiel A. Cohen,[2,23,27] Miruna Chipara,[1] Jennie Roberts,[3] Dewi Astuti,[1] Adina M. Palhegyi,[1] Animesh Acharjee,[4,5,6] Lucia Sedlackova,[7,24] Tetsushi Kataura,[7] Elsje G. Otten,[7,25] Prashanta K. Panda,[1] Samuel Lara-Reyna,[8] Miriam E. Korsgen,[1] Kevin J. Kauffman,[9,10] Alejandro Huerta-Uribe,[11] Malgorzata Zatyka,[1] Luiz F.S.E. Silva,[1] Jorge Torresi,[1] Shupei Zhang,[2] Georgina W. Hughes,[1] Carl Ward,[1]

(Author list continued on next page)

[1]Institute of Cancer and Genomic Sciences, Institute of Biomedical Research, College of Medical and Dental Sciences, University of Birmingham, Edgbaston, Birmingham B15 2TT, UK
[2]Whitehead Institute for Biomedical Research, Massachusetts Institute of Technology, Cambridge, MA 02142, USA
[3]Institute of Metabolism and Systems Research, College of Medical and Dental Sciences, University of Birmingham, Edgbaston, Birmingham B15 2TT, UK
[4]Institute of Cancer and Genomic Sciences, Centre for Computational Biology, University of Birmingham, Birmingham B15 2TT, UK
[5]Institute of Translational Medicine, University Hospitals Birmingham, NHS Foundation Trust, Birmingham B15 2TT, UK
[6]NIHR Surgical Reconstruction and Microbiology Research Centre, University Hospital Birmingham, Birmingham B15 2WB, UK
[7]Biosciences Institute, Faculty of Medical Sciences, Newcastle University, Newcastle upon Tyne NE4 5PL, UK
[8]Institute of Microbiology and Infection, University of Birmingham, Birmingham B15 2TT, UK
[9]David H. Koch Institute for Integrative Cancer Research, Massachusetts Institute of Technology, Cambridge, MA 02139, USA
[10]Department of Chemical Engineering, Massachusetts Institute of Technology, Cambridge, MA 02142, USA
[11]Wolfson Wohl Cancer Research Centre, Institute of Cancer Sciences, University of Glasgow, Glasgow G61 1QH, UK
[12]Michael Smith Laboratories, University of British Columbia, Vancouver, BC V6T 1Z4, Canada
[13]Department of Neurology, Mayo Clinic, Rochester, MN 55901, USA
[14]Department of Pharmaceutical Sciences and Department of Biomedical Engineering, College of Pharmacy, Oregon State University, Portland, OR 97201, USA
[15]Department of Developmental Biology and Cancer Research, The Institute for Medical Research Israel-Canada, The Hebrew University-Hadassah Medical School, Jerusalem 91120, Israel
[16]Department for Biosciences, Nottingham Trent University, Nottingham NG11 8NS, UK
[17]Institute for Medical Engineering and Science, Massachusetts Institute of Technology, Cambridge, MA 02139, USA
[18]Harvard and MIT Division of Health Science and Technology, Massachusetts Institute of Technology, Cambridge, MA 02139, USA
[19]Department of Endocrinology, Birmingham Women's and Children's Hospital, Steelehouse Lane, Birmingham B4 6NH, UK

(Affiliations continued on next page)

SUMMARY

Autophagy is a homeostatic process critical for cellular survival, and its malfunction is implicated in human diseases including neurodegeneration. Loss of autophagy contributes to cytotoxicity and tissue degeneration, but the mechanistic understanding of this phenomenon remains elusive. Here, we generated autophagy-deficient (*ATG5*$^{-/-}$) human embryonic stem cells (hESCs), from which we established a human neuronal platform to investigate how loss of autophagy affects neuronal survival. *ATG5*$^{-/-}$ neurons exhibit basal cytotoxicity accompanied by metabolic defects. Depletion of nicotinamide adenine dinucleotide (NAD) due to hyperactivation of NAD-consuming enzymes is found to trigger cell death via mitochondrial depolarization in *ATG5*$^{-/-}$ neurons. Boosting intracellular NAD levels improves cell viability by restoring mitochondrial bioenergetics and proteostasis in *ATG5*$^{-/-}$ neurons. Our findings elucidate a mechanistic link between autophagy deficiency and neuronal cell death that can be targeted for therapeutic interventions in neurodegenerative and lysosomal storage diseases associated with autophagic defect.

INTRODUCTION

Macroautophagy, herein referred to as autophagy, is a catabolic process encompassing the formation of autophagosomes and their fusion with lysosomes where the autophagic cargo is degraded. This process plays a fundamental role in cellular and energy homeostasis via the clearance of undesirable macromolecules and organelles and via the utilization of the

Erich R. Kuechler,[12] David Cartwright,[3] Sergey Trushin,[13] Eugenia Trushina,[13] Gaurav Sahay,[14] Yosef Buganim,[15] Gareth G. Lavery,[16] Joerg Gsponer,[12] Daniel G. Anderson,[9,10,17,18] Eva-Maria Frickel,[8] Tatiana R. Rosenstock,[1,26] Timothy Barrett,[1,19] Oliver D.K. Maddocks,[11] Daniel A. Tennant,[3] Haoyi Wang,[20] Rudolf Jaenisch,[2,21] Viktor I. Korolchuk,[7,*] and Sovan Sarkar[1,28,*]

[20]The State Key Laboratory of Stem Cell and Reproductive Biology, Institute of Zoology, Chinese Academy of Sciences, Chaoyang District, Beijing 100101, China
[21]Department of Biology, Massachusetts Institute of Technology, Cambridge, MA 02142, USA
[22]Present address: NMN Bio, Ltd., Birmingham, UK
[23]Present address: Wanda Fish Technologies, Ltd., Ness Ziona, Israel
[24]Present address: Center for Genomic Regulation, The Barcelona Institute of Science and Technology, Barcelona, Spain
[25]Present address: Amphista Therapeutics, Ltd., Cambridge, UK
[26]Present address: Sygnature Discovery, Nottingham, UK
[27]These authors contributed equally
[28]Lead contact
*Correspondence: viktor.korolchuk@newcastle.ac.uk (V.I.K.), s.sarkar@bham.ac.uk (S.S.)
https://doi.org/10.1016/j.celrep.2023.112372

breakdown products in metabolic pathways.[1–3] These functions of autophagy are vital for cell survival and pertinent for post-mitotic cells like neurons where the damaged cellular components are not diluted by cell proliferation.[4] Genetic studies in mouse models demonstrated that brain-specific abrogation of basal autophagy by inducible knockout of essential autophagy genes like *Atg5* or *Atg7* causes neurodegeneration,[5,6] implying that basal autophagy is essential for neuronal homeostasis. Similarly in other organisms, suppression of autophagy by deletion or downregulation of *atg5* reduced the lifespan in *Drosophila melanogaster* and the survival in *Saccharomyces cerevisiae* under starvation conditions.[7,8] Indeed, dysregulation of autophagy has been reported in myriad human diseases including neurodegenerative and lysosomal storage disorders, where defective autophagy is implicated as a contributing factor to the disease pathology.[9–14]

Despite the biomedical importance of autophagy in pathological contexts including neurodegeneration, it is not clear how malfunction of autophagy causes cytotoxicity. In order to mechanistically elucidate this causal link in a manner relevant to human biology, we established human cellular platforms with autophagy deficiency by utilizing human embryonic stem cells (hESCs). Unlike immortalized cells, the hESCs provide a more physiologically relevant *in vitro* experimental system because they are capable of self-renewal and also, being pluripotent, are able to differentiate into a range of human cell types like neurons.[15,16]

RESULTS

Generation and characterization of autophagy-deficient hESCs

Loss of autophagy can be achieved by knockout of *ATG5*, which encodes for a key protein required for autophagosome formation.[17] We generated autophagy-deficient ($ATG5^{-/-}$) hESCs by knockout of *ATG5* exon 3 via genome editing with transcription activator-like effector nucleases (TALENs) (Figures 1A and S1A). The correctly targeted clones were confirmed by southern blot and Sanger sequencing. We obtained homozygous ($ATG5^{-/-}$) and heterozygous ($ATG5^{+/-}$) knockout clones (Figure S1B), which expressed pluripotency markers (Figures 1B and S1C–S1E) and maintained proliferative capacity (Figures S1F and S1G) comparable to wild-type (WT; $ATG5^{+/+}$) hESCs. Since ATG5 protein normally exists in conjugation with ATG12,[18] immunoblotting analysis revealed complete or partial loss of the ATG5-ATG12 conjugate in $ATG5^{-/-}$ and $ATG5^{+/-}$ hESCs, respectively (Figures 1C and S1H). Loss of autophagy was demonstrated under basal and starvation conditions in multiple clones of $ATG5^{-/-}$ hESCs via the absence of autophagosomes (lack of $LC3^{+}$ puncta, LC3-II levels, or autophagic vacuoles) and an accumulation of autophagy substrate (increased p62/SQSTM1 levels) (Figures 1C, 1D, S1H, and S1I). Moreover, starvation-induced autophagy was observed in WT, but not in $ATG5^{-/-}$, hESCs (Figures 1C, 1D, and S1H).

To further validate our genetic hESC model, we complemented $ATG5^{-/-}$ hESCs with human *ATG5* mRNA via lipid nanoparticles (LNPs), formulated with the ionizable lipid C12-200,[19] to restore functional autophagic flux (Figure S1J). Introduction of C12-200 LNP-encapsulated human *ATG5* mRNA, but not *GFP* mRNA, into $ATG5^{-/-}$ hESCs generated the ATG5-ATG12 conjugate, thus enabling autophagosome formation (LC3 lipidation) and p62 clearance (Figure 1E). Next, we analyzed whether loss of autophagy in hESCs affected their survival. Increased apoptosis in $ATG5^{-/-}$ hESCs was evident from elevated levels of cleaved caspase-3 and luminescence-based cytotoxicity assay under normal growth conditions (Figures 1F and 1G), indicating that autophagy deficiency impairs cell viability in hESCs.

Autophagy-deficient human neurons manifest with elevated cell death

We further sought to establish human neurons with autophagy deficiency to investigate whether and how loss of autophagy affects neuronal survival. $ATG5^{+/+}$ and multiple clones of $ATG5^{-/-}$ hESCs were differentiated into neural precursors (NPs) via "dual-SMAD inhibition method" followed by neuronal differentiation (Figure S2A), as previously described.[20] The NPs derived via this method carry an anterior identity and commit to forebrain fates when cultured in the presence of bFGF and EGF.[21] The cellular identity of hESC-derived NPs and neurons was confirmed by the expression of their cell-specific markers, which were comparable between the WT and $ATG5^{-/-}$ cells (Figures 2A and S2B–S2E). Autophagy deficiency was confirmed in $ATG5^{-/-}$ NPs and neurons via the lack of ATG5-ATG12 conjugate and LC3-II

CellPress
OPEN ACCESS

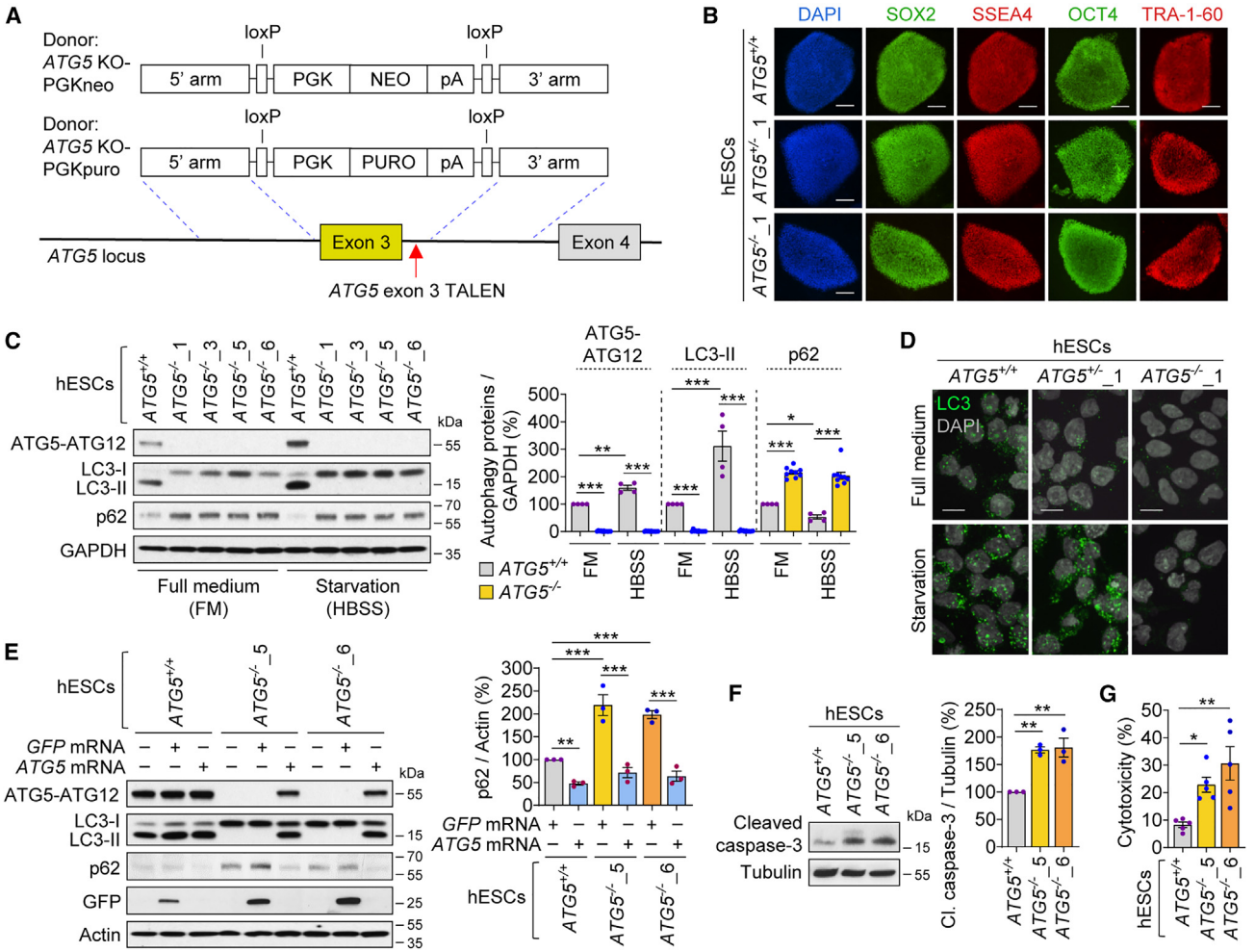

Figure 1. Loss of autophagy and increased cell death in *ATG5*$^{-/-}$ hESCs

(A) Targeting strategy for deleting exon 3 in human *ATG5* gene by TALENs.

(B–D) Immunofluorescence images of SOX2, SSEA4, OCT4, and TRA-1-60 (B), immunoblotting analyses of ATG5, LC3, and p62 (C), and immunofluorescence images of LC3 puncta (D) in *ATG5*$^{+/+}$, *ATG5*$^{+/-}$_1, and multiple clones of *ATG5*$^{-/-}$ hESCs, cultured in full growth medium (FM) (B–D) or starvation condition (HBSS for 3 h) (C and D).

(E) Immunoblotting analyses of ATG5, LC3, p62, and GFP in *ATG5*$^{+/+}$, *ATG5*$^{-/-}$_5, and *ATG5*$^{-/-}$_6 hESCs, treated for 4 days with or without C12-200 lipid nanoparticle (LNP)-containing 2 μg/mL *GFP* or *ATG5* mRNA.

(F and G) Immunoblotting analysis of cleaved caspase-3 (F) and cytotoxicity assay (G) in *ATG5*$^{+/+}$, *ATG5*$^{-/-}$_5, and *ATG5*$^{-/-}$_6 hESCs.

Graphical data are mean ± SEM of n = 3–11 biological replicates as indicated. p values were calculated by one-way ANOVA followed by multiple comparisons with two-stage linear step-up procedure of Benjamini, Krieger, and Yekutieli on 3 independent experiments (C and E–G). ***p < 0.001; **p < 0.01; *p < 0.05. Scale bars: 100 μm (D) and 200 μm (B).

See also Figure S1.

levels/puncta and via p62 accumulation (Figures 2B–2D and S2F). Further validation of the human neuronal platform was made by LNP-mediated mRNA delivery (Figures 2E and S1J). Initial evaluation of C12-200 LNPs for *GFP* mRNA delivery showed efficient GFP expression in hESC-derived neurons (Figure S2G). As in *ATG5*$^{-/-}$ hESCs, C12-200 LNP-mediated delivery of human *ATG5* mRNA, but not GFP mRNA, restored functional autophagic flux in *ATG5*$^{-/-}$ neurons (Figures 2E and S2H).

To assess whether loss of autophagy in human neurons compromises cellular viability, we analyzed cell death at the population and single-cell levels. *ATG5*$^{-/-}$ NPs and neurons exhibited elevation in cleaved caspase-3 levels under basal condition compared with their WT counterparts (Figures 2F and S2I). Additionally, TUJ1^{+} *ATG5*$^{-/-}$ neurons displayed significantly more TUNEL^{+} apoptotic nuclei and DAPI-stained apoptotic nuclear morphology compared with *ATG5*$^{+/+}$ neurons (Figures 2G, 2H, S2J, and S2K). Increased cytotoxicity was observed in *ATG5*$^{-/-}$ neurons as early as at 2 weeks of neuronal differentiation, and this was more substantial after 4 weeks (Figure 2I). Altogether, the cell death phenotypes in autophagy-deficient hESCs and NPs appear to become further pronounced following their differentiation to neurons.

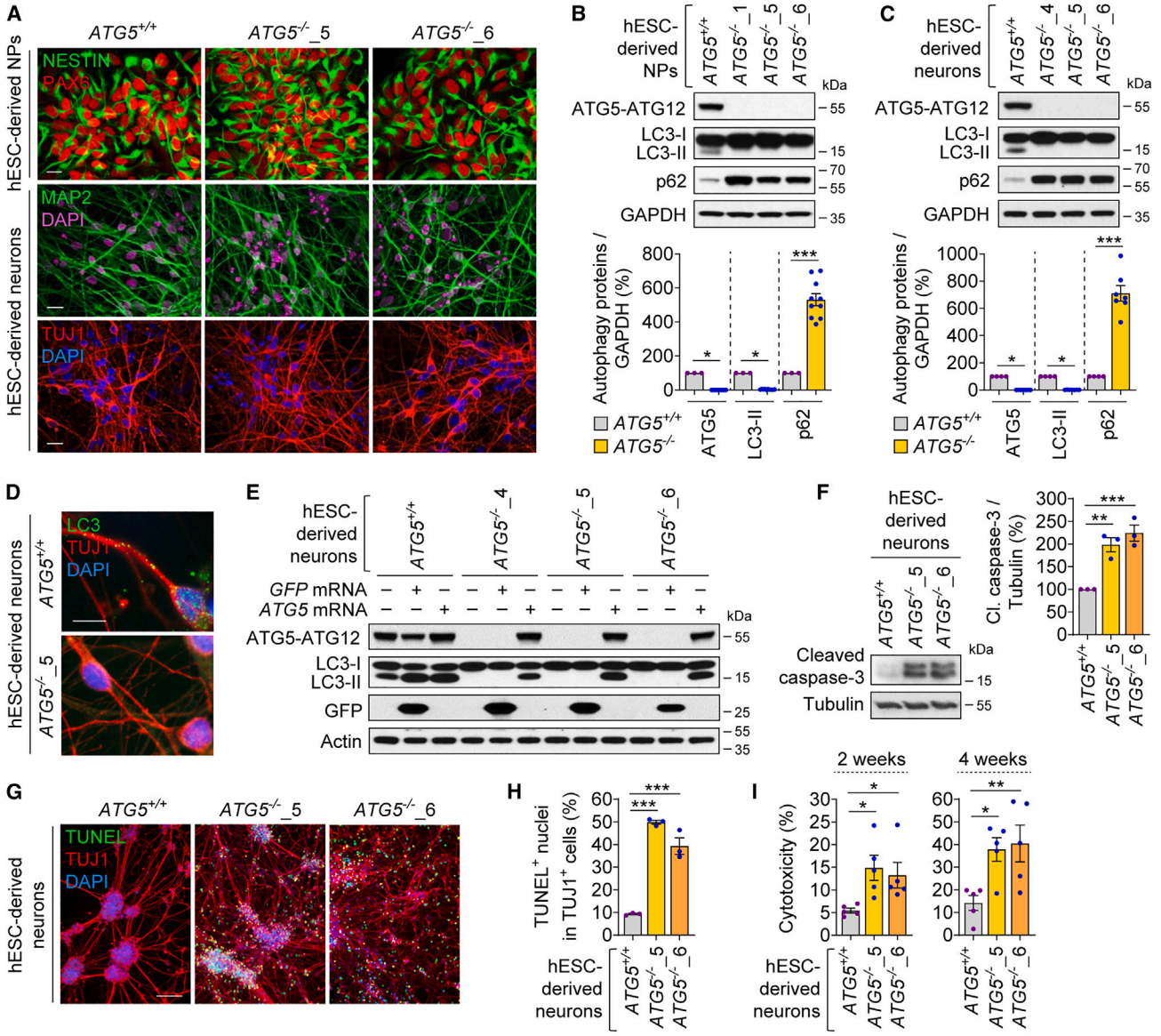

Figure 2. Autophagy deficiency and increased cell death in *ATG5*$^{-/-}$ NPs and neurons

(A–D) Immunofluorescence images of NESTIN, PAX6, MAP2, and TUJ1 (A), immunoblotting analyses of ATG5, LC3, and p62 (B and C), and immunofluorescence images of LC3 puncta and TUJ1 (D) in *ATG5*$^{+/+}$ and multiple clones of *ATG5*$^{-/-}$ hESC-derived NPs (A and B) and neurons (4 weeks) (A and C).

(E) Immunoblotting analyses of ATG5, LC3, and GFP in *ATG5*$^{+/+}$ and multiple clones of *ATG5*$^{-/-}$ hESC-derived neurons (4 weeks), treated for 4 days with or without C12-200 LNP-containing 2 μg/mL *GFP* or *ATG5* mRNA.

(F–I) Immunoblotting analysis of cleaved caspase-3 (F), immunofluorescence images of TUJ1 with TUNEL staining (G), and quantification of TUNEL^{+} apoptotic nuclei (H) and cytotoxicity assay (I) in *ATG5*$^{+/+}$, *ATG5*$^{-/-}$_5, and *ATG5*$^{-/-}$_6 hESC-derived neurons at 2 (I) or 4 weeks (F–I) of neuronal differentiation.

Graphical data are mean ± SEM of n = 3–10 biological replicates as indicated. p values were calculated by one-way ANOVA followed by multiple comparisons with two-stage linear step-up procedure of Benjamini, Krieger, and Yekutieli on 3 independent experiments (B, C, F, H, and I). ***p < 0.001; **p < 0.01; *p < 0.05. Scale bars: 10 μm (D) and 100 μm (A and G).

See also Figure S2.

Metabolic perturbations in autophagy-deficient human neurons

We next endeavored to investigate what cellular mechanisms underlying cell death are primarily affected due to autophagy deficiency in human neurons. Since *ATG5*$^{-/-}$ hESCs and hESC-derived NPs and neurons exhibited cytotoxicity at basal state, we hypothesized that this might arise from a metabolic failure. Autophagy promotes metabolic homeostasis by recycling cytoplasmic macromolecules and providing the breakdown products as inputs to cellular anabolic processes, failure of which could lead to metabolic stress.[3,22] Although depletion of several metabolites, amino acids, and nucleotides associated

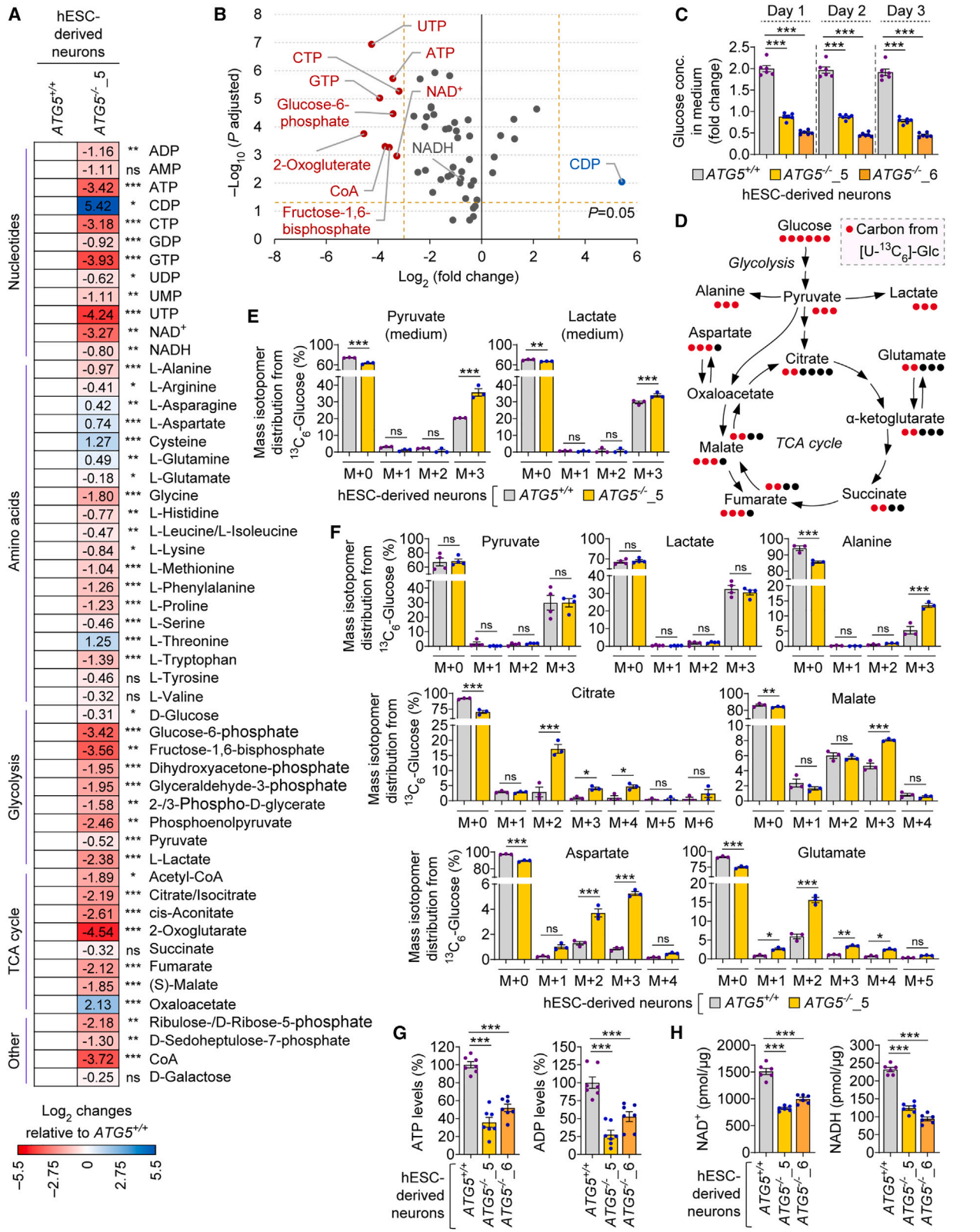

(legend on next page)

with the loss of autophagy has been reported in immortalized cells and mouse models,[2,23] the mechanistic link between these metabolic defects and cell death is unclear.

To investigate any specific metabolic defect in our experimental system, we performed an unbiased metabolomics profiling of WT and *ATG5*$^{-/-}$ hESC-derived neurons. Significant depletion of several metabolites related to glycolysis and tricarboxylic acid (TCA) cycle, nucleotide energy carriers, and various amino acids was detected in *ATG5*$^{-/-}$ neurons (Figures 3A, S3A, and S3B). By plotting the magnitude of change against the measure of significance, several nucleotides were found to be significantly depleted in *ATG5*$^{-/-}$ neurons (Figure 3B). This is in accordance with the nucleic acid recycling defect reported in autophagy-deficient tumor-derived cell lines.[23] Alongside this, some of the intermediates of glycolysis and TCA cycle were also significantly lower in *ATG5*$^{-/-}$ neurons (Figure 3B). These findings suggest that autophagy-deficient human neurons are associated with metabolic stress under normal growth condition.

Depletion of ATP and NAD(H) in autophagy-deficient neurons despite compensatory increase in glucose metabolism

Metabolomics data implied that glycolysis and TCA cycle are affected because the steady-state levels of the respective starting molecule, such as glucose and acetyl-coenzyme A (CoA), as well as several other intermediates, were reduced in *ATG5*$^{-/-}$ neurons (Figures 3A, S3A, and S3C). However, glucose uptake was significantly higher in *ATG5*$^{-/-}$ neurons (Figures 3C and S3D), suggesting that intracellular glucose could be rapidly metabolized through the glycolytic pathway. We further employed [U-$^{13}C_6$]-Glucose tracer to elucidate the contribution of glucose to glycolysis and TCA cycle (Figure 3D). Glycolysis breaks the glucose carbon skeleton into three carbon units in the form of pyruvate, which can then undergo several metabolic transformations. These include lactate, alanine, oxaloacetate, and the two-carbon unit acetyl-CoA that can enter the TCA cycle, condensing with oxaloacetate to form citrate (Figure 3D).[24] The pattern of ^{12}C and ^{13}C carbons in each metabolite provides information on the active metabolic pathways. Both lactate and pyruvate were secreted into the medium with a higher fraction of the M+3 isotopomer in *ATG5*$^{-/-}$ neurons (Figure 3E), demonstrating a greater contribution of glucose-derived carbons from the glycolytic pathway. Likewise, intracellular alanine also had an elevated fraction of the M+3 isotopomer in *ATG5*$^{-/-}$ neurons (Figure 3F). Labeling patterns of the TCA cycle intermediates such as citrate, α-ketoglutarate, succinate, fumarate, and malate included both the M+2 and M+3 isotopomers, indicating that a higher fraction of glucose-derived pyruvate was incorporated via both acetyl CoA and oxaloacetate in *ATG5*$^{-/-}$ neurons (Figures 3D, 3F, and S3E). The amino acids aspartate and glutamate also contained a glucose-derived ^{13}C label that mirrored the labeling of malate and citrate, respectively, indicating that the synthesis of both these metabolites involved a greater contribution from glucose in *ATG5*$^{-/-}$ neurons (Figures 3D and 3F). Collectively, our data show a greater use of glucose in central carbon metabolism in autophagy-deficient neurons as an attempt to cope with their metabolic stress. However, despite this compensation, the reduction in almost all TCA cycle metabolites suggests that this response is insufficient to ameliorate the loss of autophagy-derived metabolites from the metabolic network.

The overall yield from glycolysis and TCA cycle normally constitutes ATP and NADH.[25] Despite increased glucose contribution to these metabolic pathways, unbiased metabolomics data revealed significant depletion of ATP, ADP, NAD^+, and NADH levels in *ATG5*$^{-/-}$ neurons (Figures 3A, 3B, S3A, S3F, and S3G), which was further confirmed by specific luminescence- and colorimetric-based assays (Figures 3G and 3H). Since depletion of energy carriers like ATP and NADH could trigger energetic deficit,[25] it is likely that the autophagy-deficient neurons are attempting to restore their levels by utilizing more glucose through glycolysis and TCA cycle. Interestingly, *ATG5*$^{-/-}$ hESCs exhibited substantial elevation in ATP and ADP levels, although they had lower NAD^+ and NADH levels compared with WT hESCs (Figures S3H and S3I). This is likely due to cell-specific metabolic requirements, since proliferating hESCs rely on glycolysis for energy production and pluripotency but, upon differentiation, switch to mitochondrial oxidative phosphorylation.[26] These data indicate that among the major energy carriers, NAD(H) depletion during loss of autophagy is common in proliferating hESCs and post-mitotic neurons associated with increased cytotoxicity.

Supplementation of L-tryptophan restores NAD(H) levels and rescues viability of autophagy-deficient neurons

Apart from nucleotides and various intracellular metabolites, unbiased metabolomics profiling also revealed significant depletion of several amino acids in *ATG5*$^{-/-}$ neurons (Figures 3A and S3A). By plotting the magnitude of change of all the amino acids against their measure of significance,

Figure 3. Metabolic perturbations in *ATG5*$^{-/-}$ neurons

(A and B) Metabolic profiling depicted as heatmap of $\log_2$ (fold change) (A), and volcano plot representation of all analyzed metabolites (thresholds shown as dashed orange lines) (B), in a pairwise comparison of *ATG5*$^{-/-}$_5 with *ATG5*$^{+/+}$ hESC-derived neurons (3 weeks).

(C) Measurement of glucose concentration in medium (fold change from day 0) of *ATG5*$^{+/+}$ and *ATG5*$^{-/-}$ hESC-derived neurons (3 weeks).

(D) Schematic representation of carbon atom (circles) transitions from [U-$^{13}C_6$]-glucose tracer to determine the contribution of glucose to glycolysis and TCA cycle.

(E and F) Mass isotopomer distribution from [U-$^{13}C_6$]-glucose in various glycolysis and TCA cycle intermediates as indicated, measured in the medium (E) or cell extract (F) of *ATG5*$^{+/+}$ and *ATG5*$^{-/-}$ hESC-derived neurons (3 weeks) by GC-MS.

(G and H) Measurements of ATP and ADP (G) and NAD^+ and NADH (H) levels in *ATG5*$^{+/+}$ and *ATG5*$^{-/-}$ hESC-derived neurons (3 weeks).

Graphical data are mean ± SEM of n = 3–7 biological replicates as indicated. p values were calculated by Student's t test using Benjamini and Hochberg false discovery rate (FDR) method (A and B) or one-way ANOVA followed by multiple comparisons with two-stage linear step-up procedure of Benjamini, Krieger, and Yekutieli (C and E–H) on 3 independent experiments. ***$p < 0.001$; **$p < 0.01$; *$p < 0.05$; ns (non-significant).

See also Figure S3 and Table S1.

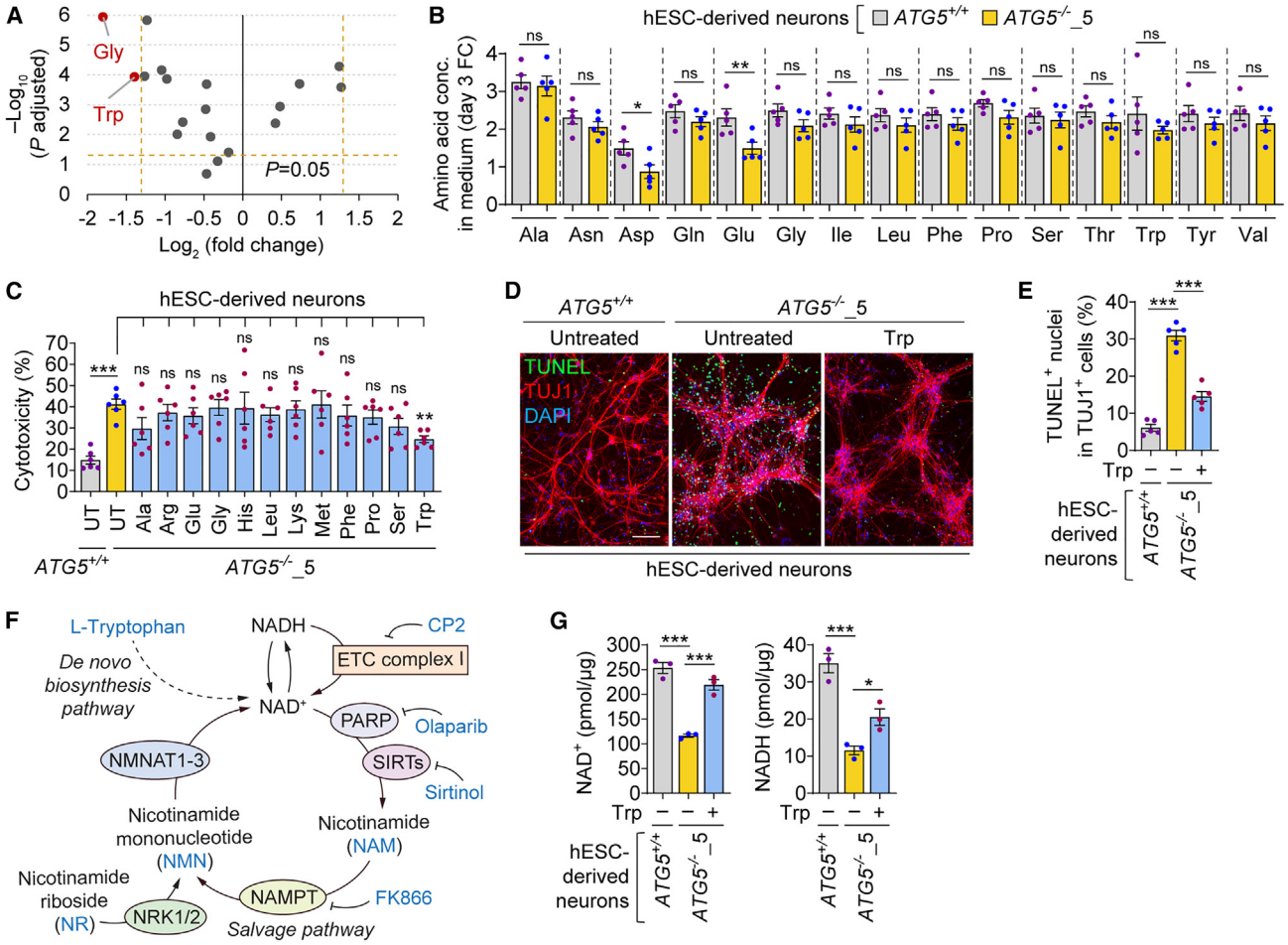

Figure 4. L-tryptophan supplementation rescues NAD(H) levels and cell viability in *ATG5*$^{-/-}$ neurons

(A) Volcano plot representation of all amino acids in a pairwise comparison of *ATG5*$^{-/-}$ with *ATG5*$^{+/+}$ hESC-derived neurons (3 weeks); thresholds shown as dashed orange lines.

(B) Measurement of amino acid concentrations (fold change at day 3) in medium of *ATG5*$^{+/+}$ and *ATG5*$^{-/-}$ hESC-derived neurons (3 weeks) by GC-MS.

(C) Cytotoxicity assay in *ATG5*$^{+/+}$ and *ATG5*$^{-/-}$ hESC-derived neurons (3 weeks), where *ATG5*$^{-/-}$ neurons were treated with or without 1 mM individual amino acid as indicated for the last 6 days of neuronal differentiation period.

(D and E) Immunofluorescence images of TUJ1 with TUNEL staining (D) and quantification of TUNEL^{+} apoptotic nuclei (E) in *ATG5*$^{+/+}$ and *ATG5*$^{-/-}$_5 hESC-derived neurons (3 weeks), where *ATG5*$^{-/-}$ neurons were treated with or without 1 mM L-tryptophan (Trp) for the last 6 days of neuronal differentiation period.

(F) Schematic representation of NAD^{+} *de novo* biosynthetic and salvage pathways where compounds used for modulating NAD(H) levels are indicated.

(G) Measurements of NAD^{+} and NADH levels in *ATG5*$^{-/-}$ hESC-derived neurons (3 weeks), treated with or without 1 mM L-Trp for the last 6 days of neuronal differentiation period.

Graphical data are mean ± SEM of n = 3–6 biological replicates as indicated. p values were calculated by Student's t test using Benjamini and Hochberg FDR method (A) or one-way ANOVA followed by multiple comparisons with two-stage linear step-up procedure of Benjamini, Krieger, and Yekutieli (B, C, E, and G) on 3 independent experiments. ***p < 0.001; **p < 0.01; *p < 0.05; ns (non-significant). Scale bar: 100 µm (D).

See also Figure S4.

glycine and L-tryptophan were found to be most significantly depleted in *ATG5*$^{-/-}$ neurons (Figure 4A). However, individual amino acid uptake was not overtly different between *ATG5*$^{-/-}$ and WT neurons as measured by the fold change of amino acid concentrations in the medium, except for increased uptake of L-aspartate and L-glutamate in *ATG5*$^{-/-}$ neurons (Figures 4B and S4A–S4C), indicating higher reliance on these amino acids. Both amino acids are excitatory neurotransmitters,[27] and their increased uptake in *ATG5*$^{-/-}$ neurons could be due to higher metabolic demand in TCA cycle as revealed by [U-$^{13}C_6$]-glucose tracer (Figures 3D and 3F).

We next analyzed whether supplementation with each of the 12 amino acids, which were significantly depleted as per unbiased metabolomics (Figures 3A and S3A), could rescue the viability of *ATG5*$^{-/-}$ neurons. Interestingly, only supplementation of L-tryptophan, which was depleted in these cells (Figures 3A, 4A, S3A, and S4D), significantly reduced cytotoxicity in *ATG5*$^{-/-}$ neurons (Figure 4C). The cytoprotective effect

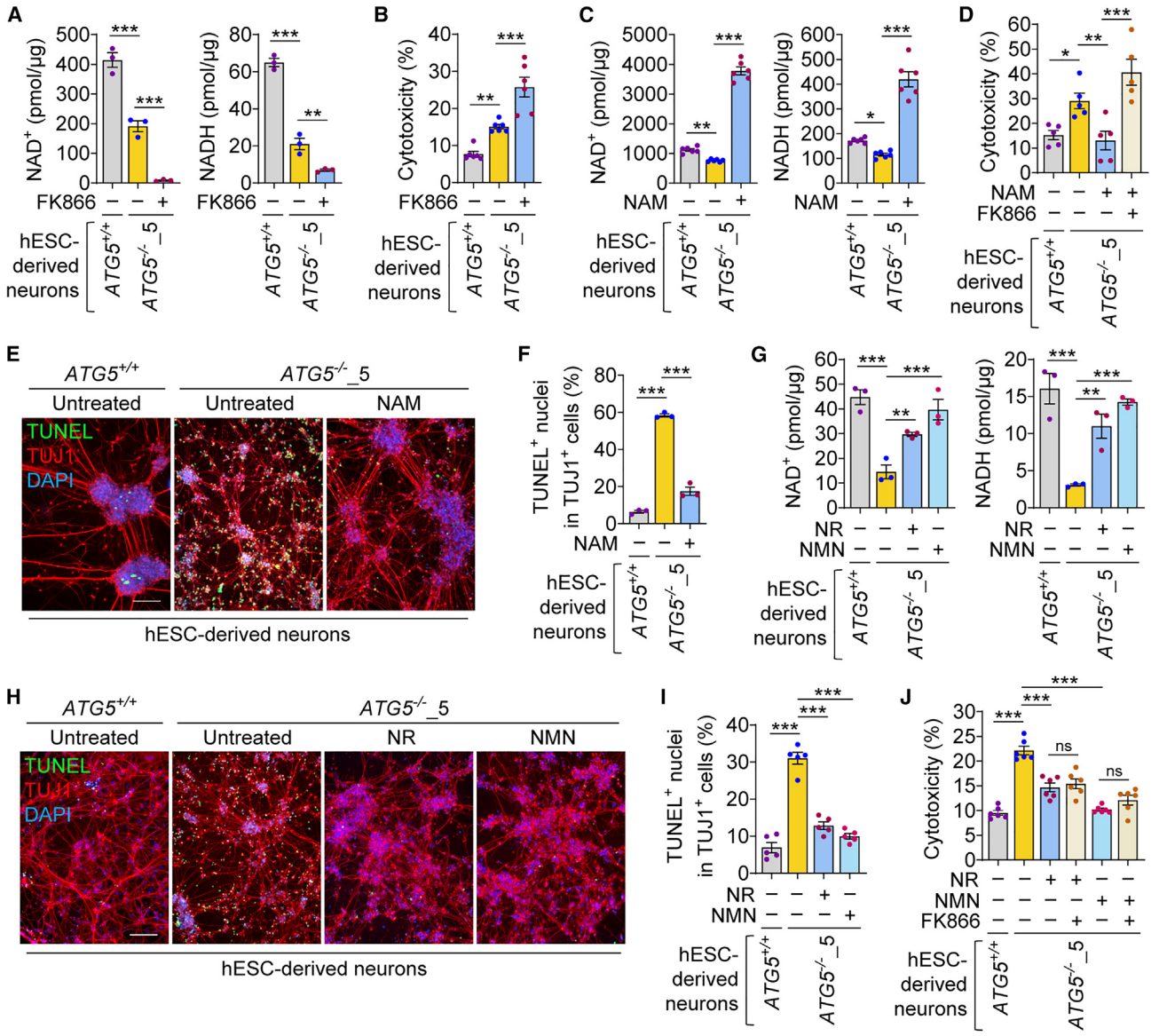

Figure 5. Modulation of NAD(H) levels affects cell viability in *ATG5*$^{-/-}$ neurons

(A–J) Measurements of NAD$^+$ and NADH levels (A, C, and G), cytotoxicity assay (B, D, and J), immunofluorescence images of TUJ1 with TUNEL staining (E and H), and quantification of TUNEL$^+$ apoptotic nuclei (F and I) in *ATG5*$^{+/+}$ and *ATG5*$^{-/-}$_5 hESC-derived neurons (3 weeks), where *ATG5*$^{-/-}$ neurons were treated with or without 10 nM FK866 (A, B, D, and J), 1 mM NAM (C–F), 1 mM NR (G–J), or 1 mM NMN (G–J) as indicated for the last 6 days of neuronal differentiation period. Graphical data are mean ± SEM of n = 3–6 biological replicates as indicated. p values were calculated by one-way ANOVA followed by multiple comparisons with two-stage linear step-up procedure of Benjamini, Krieger, and Yekutieli on 3 independent experiments (A–D, F, G, I, and J). ***p < 0.001; **p < 0.01; *p < 0.05; ns (non-significant). Scale bar: 100 µm (E and H).

See also Figure S5.

of L-tryptophan supplementation was further confirmed by reduction of TUNEL$^+$ apoptotic nuclei in TUJ1$^+$ *ATG5*$^{-/-}$ neurons (Figures 4D and 4E). L-tryptophan is required for the *de novo* synthesis of NAD via the kynurenine pathway (Figures 4F),[28] and hence it could impact cell survival by modulating NAD(H) levels that were depleted in *ATG5*$^{-/-}$ neurons (Figures 3A, 3B, 3H, and S3G). Concomitant to reducing cell death, L-tryptophan supplementation significantly restored NAD(H) levels in *ATG5*$^{-/-}$ neurons (Figure 4G), raising the possibility that NAD(H) levels could affect the viability of autophagy-deficient human neurons.

Boosting intracellular NAD(H) improves viability of autophagy-deficient neurons

We next investigated a potential role of NAD(H) in mediating cytotoxicity in human neurons with autophagy deficiency. NAD$^+$ (the oxidized form of NAD) was one of the most depleted metabolites in *ATG5*$^{-/-}$ neurons, whereas NADH (the reduced

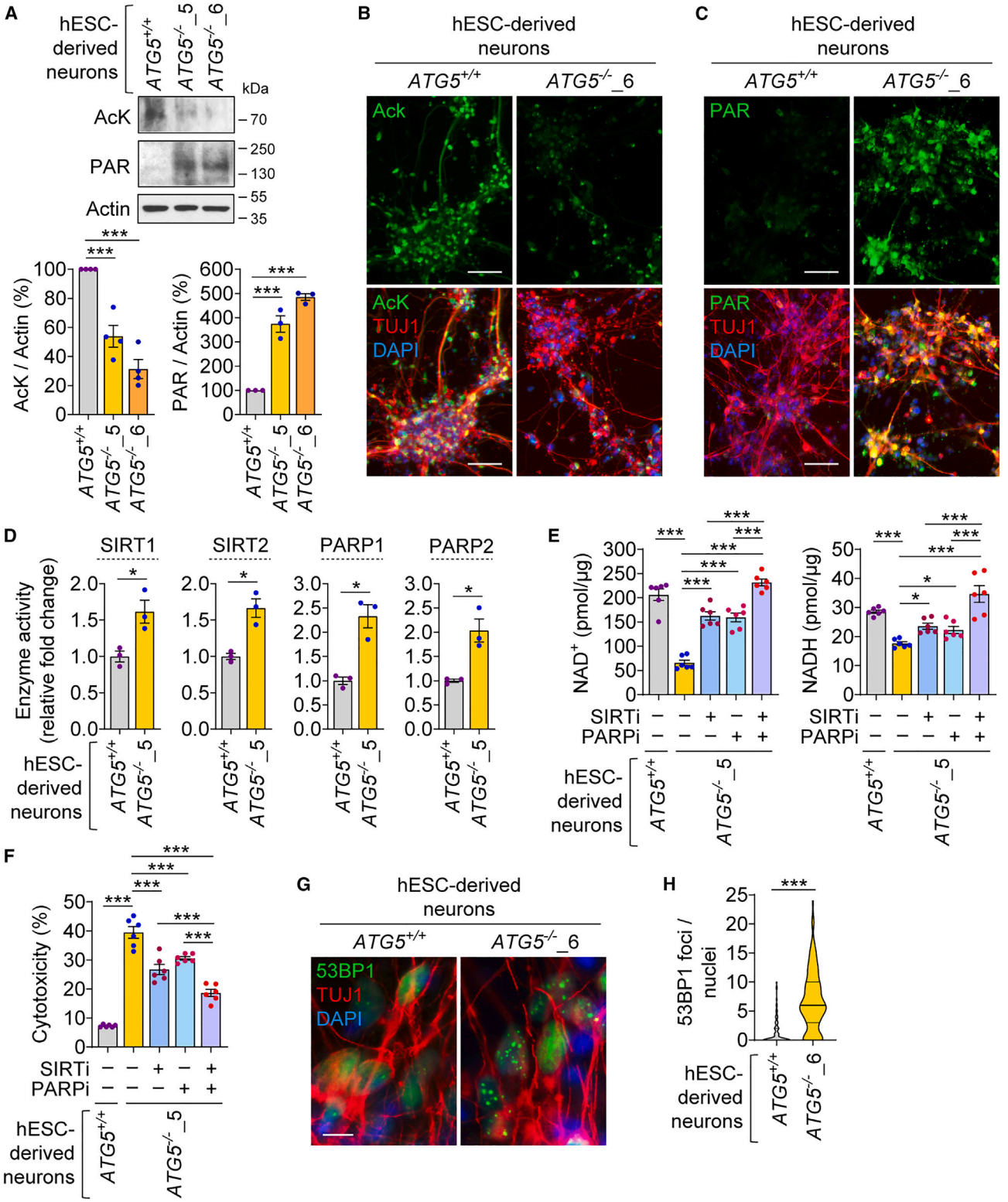

Figure 6. Hyperactivation of NADases mediates NAD(H) depletion in *ATG5*$^{-/-}$ neurons

(A–D) Immunoblotting analyses of acetylated lysine (AcK) and poly(ADP-ribose) (PAR) (A), immunofluorescence images of TUJ1 with AcK (B) or PAR (C), and enzymatic activity of SIRT1, SIRT2, PARP1, and PARP2 (D) in *ATG5*$^{+/+}$ and *ATG5*$^{-/-}$ hESC-derived neurons (3 weeks).

(legend continued on next page)

form of NAD) was also significantly lower, indicating exhaustion of the total pool of NAD(H) (Figures 3A, 3B, 3H, S3A, and S3G). We initially assessed whether preventing NAD production affects cell viability by the inhibition of nicotinamide phosphoribosyltransferase (NAMPT), which is involved in NAD biosynthesis via a salvage pathway, with FK866 (Figure 4F).[29] The NAMPT inhibitor FK866 markedly lowered NAD(H) levels and compromised the viability of *ATG5*$^{-/-}$ neurons (Figures 5A, 5B, S5A, and S5B). Conversely, we assessed if boosting intracellular NAD(H) levels can rescue cell viability. A well-known strategy is supplementation with the bioavailable NAD precursor nicotinamide (NAM) (Figures 4F),[30,31] which substantially increased NAD(H) levels and improved cell viability in *ATG5*$^{-/-}$ neurons (Figures 5C–5F). We also observed reduction in axonal length in *ATG5*$^{-/-}$ neurons compared with *ATG5*$^{+/+}$ neurons, and this morphological defect was concomitantly rescued by NAM (Figures S5C and S5D). Similarly, NAM restored NAD(H) levels and improved cell viability in *ATG5*$^{-/-}$ hESCs (Figures S5E and S5F). The cytoprotective effects of boosting NAD(H) in autophagy-deficient cells were further supported with additional NAD precursors, such as nicotinamide riboside (NR) and nicotinamide mononucleotide (NMN) (Figure 4F).[32,33] Indeed, both NR and NMN significantly restored NAD(H) levels and rescued cell viability in *ATG5*$^{-/-}$ neurons (Figures 5G–5J).

Since the NAD precursors elevated NAD(H) levels via the salvage pathway, we analyzed their dependency on NAMPT for conversion using FK866 (Figure 4F). The cytoprotective effect of NAM in rescuing the viability of *ATG5*$^{-/-}$ neurons was completely abolished by FK866 (Figure 5D); however, the effects of NR or NMN were unaffected by FK866 treatment (Figure 5J). This is likely because NAMPT is required for the conversion of NAM to NAD^+, whereas NR and NMN act downstream of NAMPT (Figure 4F). Overall, these data suggest that modulating NAD(H) levels affects cell viability and that boosting intracellular NAD(H) improves the survival of autophagy-deficient human neurons.

Increased NADase activity mediates NAD(H) depletion in autophagy-deficient neurons

We further investigated the mechanism of NAD(H) depletion in *ATG5*$^{-/-}$ neurons. NAD^+ can be degraded by NAD^+ nucleosidases (NADases) to maintain NAD^+ homeostasis.[34,35] The two main classes of NADases are deacetylases of the sirtuin family (SIRTs) and poly-ADP-ribose polymerases (PARPs), which utilize NAD^+ as a substrate (Figure 4F).[36] Activities of SIRTs and PARPs were elevated in *ATG5*$^{-/-}$ neurons and also in *ATG5*$^{-/-}$ hESCs and NPs, as evident from the reduction in protein acetylation and increase in poly-ADP-ribosylation (PARylation) of acetylated lysine and poly(ADP-ribose), respectively (Figures 6A–6C and S6A). We further measured the enzymatic activity of SIRT1, SIRT2, PARP1, and PARP2, all of which were higher in *ATG5*$^{-/-}$ neurons compared with WT neurons (Figure 6D). These data imply that hyperactivation of these NAD-consuming enzymes during loss of autophagy could deplete NAD(H) and trigger cell death. To test this possibility, we pharmacologically inhibited SIRTs and PARPs with sirtinol and olaparib, respectively (Figures 4F, S6B, and S6C). Both sirtinol and olaparib rescued NAD(H) levels and the viability of *ATG5*$^{-/-}$ neurons (Figures 6E, 6F, S6D, and S6E), suggesting that suppression of NAD(H) exhaustion increases the survival of autophagy-deficient human neurons. Simultaneous inhibition of SIRTs and PARPs in *ATG5*$^{-/-}$ neurons rescued NAD(H) levels and cell viability to a greater extent than is achieved with the inhibition of either enzyme alone (Figures 6E and 6F), thus implicating both classes of NADases in NAD(H) depletion.

PARPs and SIRTs are activated in response to DNA damage and oxidative stress, and both these NADases are involved in the regulation of genomic stability.[37] Lack of autophagy has been shown to accumulate DNA damage and cause genomic instability via impairment in DNA double-strand break repair mechanisms and inefficient turnover of p62 and nuclear components.[38] Expectedly, increased DNA damage was found in *ATG5*$^{-/-}$ neurons as evident from significantly higher numbers of γH2AX and 53BP1 foci compared with the WT neurons (Figures 6G, 6H, S6F, and S6G). These data imply that persistent DNA damage in autophagy-deficient neurons could contribute to NAD(H) depletion via activation of NAD-consuming enzymes.

NAD(H) depletion triggers cell death via mitochondrial depolarization in autophagy-deficient neurons

We next investigated the mechanistic link between NAD(H) depletion and cell death in autophagy-deficient human neurons. While NAD^+ was substantially decreased in the cytosolic fraction, NADH was predominantly detected and found to be depleted in the mitochondrial fraction of *ATG5*$^{-/-}$ neurons (Figure 7A). Oxidation of NADH mediates the generation of mitochondrial membrane potential ($\Delta\Psi_m$), in which the flow of electrons (donated by NADH) through the mitochondrial electron transport chain (ETC) coupled to proton pumping across the inner mitochondrial membrane create an electrochemical proton gradient, which eventually drives ATP production by the mitochondrial F_0F_1-ATP synthase.[39] Depletion of NADH in autophagy-deficient cells could thus dissipate $\Delta\Psi_m$ and mediate cytotoxicity.[40,41] Supporting this hypothesis, *ATG5*$^{-/-}$ neurons displayed a reduction in $\Delta\Psi_m$ as measured by TMRE fluorescence intensity (Figure 7B). Moreover, *ATG5*$^{-/-}$ neurons had elevation in reactive oxygen species (ROS) and mitochondrial fragmentation (Figures 7C–7E, S7A, and S7B), and an increase

(E and F) Measurements of NAD^+ and NADH levels (E) and cytotoxicity assay (F) in *ATG5*$^{+/+}$ and *ATG5*$^{-/-}$_5 hESC-derived neurons (3 weeks), where *ATG5*$^{-/-}$ neurons were treated with or without 20 μM sirtinol (SIRT inhibitor), 10 μM olaparib (PARP inhibitor), or both for the last 3 days of neuronal differentiation period. (G and H) Immunofluorescence images of TUJ1 with 53BP1 (G) and quantification of 53BP1 foci (H) in *ATG5*$^{+/+}$ and *ATG5*$^{-/-}$_6 hESC-derived neurons (3 weeks). Graphical data are mean ± SEM of n = 3–6 biological replicates as indicated (A and D–F) or displayed as violin plot (lines at median and quartiles) from ~200 cells per condition of n = 3 biological replicates (H). p values were calculated by one-way ANOVA followed by multiple comparisons with two-stage linear step-up procedure of Benjamini, Krieger, and Yekutieli (A, E, and F) or unpaired two-tailed Student's t test (D and H) on 3 independent experiments. ***$p < 0.001$; *$p < 0.05$. Scale bars: 10 μm (G) and 50 μm (B and C).
See also Figure S6.

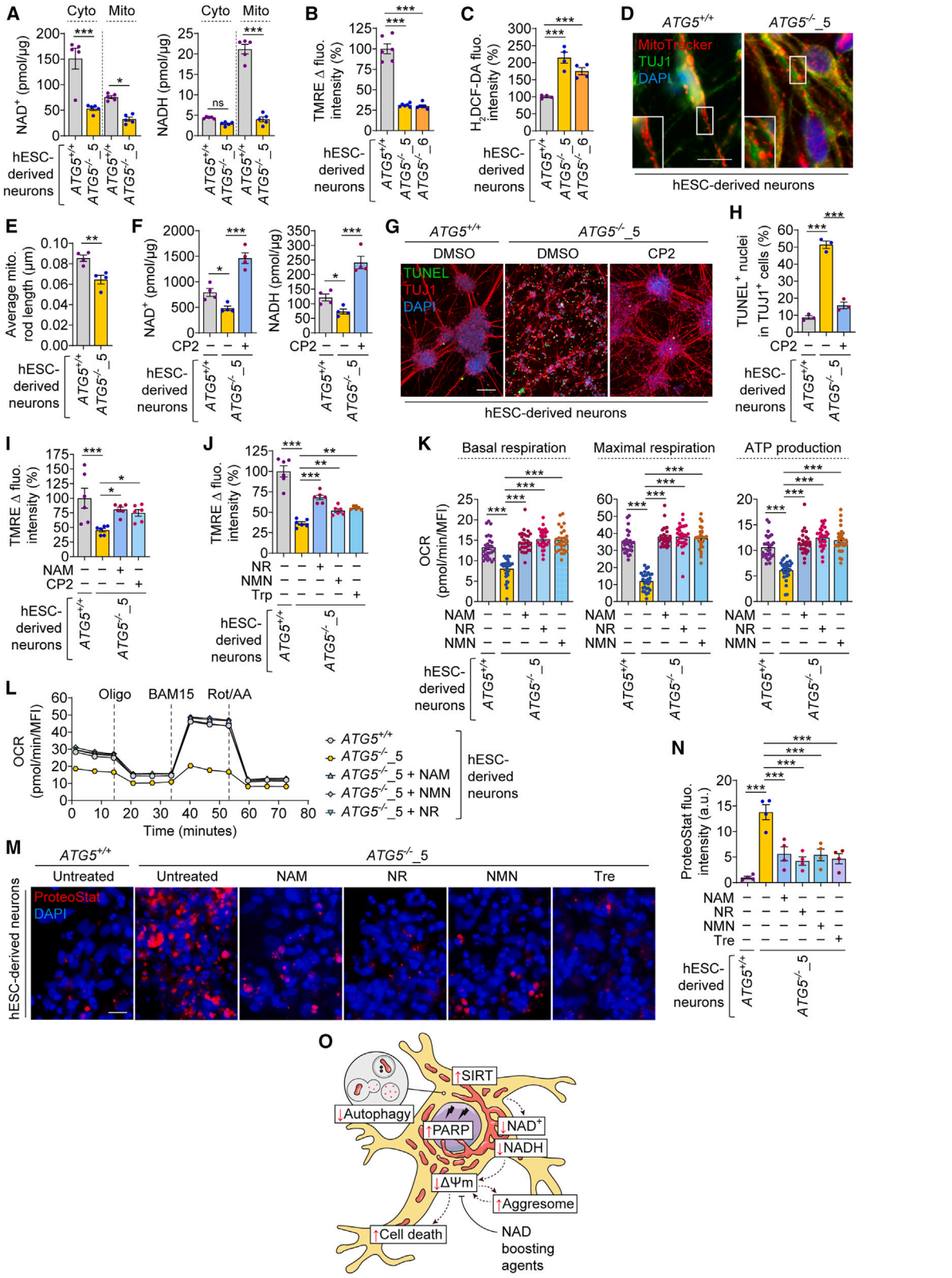

(legend on next page)

in oxidative stress could contribute to SIRT activation in these cells (Figures 6A, 6B, and 6D).[41] Similar mitochondrial dysfunction phenotypes were also found in *ATG5*$^{-/-}$ hESCs (Figures S7C–S7F). Furthermore, loss of autophagy will lead to inefficient mitophagy resulting in the accumulation of damaged mitochondria,[42] which was confirmed by the increase in mitochondrial load in *ATG5*$^{-/-}$ neurons as assessed by elevated Tom20 levels (Figure S7G). Collectively, our data raise the possibility that the deficit in NADH links autophagy deficiency to cell death via mitochondrial dysfunction and the loss of $\Delta\Psi_m$.

To test this hypothesis, we pharmacologically suppressed mitochondrial NADH consumption with CP2, which reversibly inhibits mitochondrial ETC complex I and partially suppresses the use of NADH as a substrate (Figure 4F).[43] CP2 increased NAD(H) levels and rescued cell viability in *ATG5*$^{-/-}$ neurons (Figures 7F–7H and S7H), and these cytoprotective effects were associated with the rescue of $\Delta\Psi_m$ in *ATG5*$^{-/-}$ neurons (Figure 7I). We further tested whether other NAD(H) boosting agents could attenuate mitochondrial depolarization. NAM, NR, NMN, and L-tryptophan, all of which improved NAD(H) levels and cell viability in *ATG5*$^{-/-}$ neurons (Figures 4D–4G and 5C–5J), also rescued $\Delta\Psi_m$ in these cells (Figures 7I and 7J). Furthermore, analysis of mitochondrial respiration by measuring the oxygen consumption rate showed severe impairment in *ATG5*$^{-/-}$ neurons compared with WT neurons, as seen by reduction in basal respiration, maximal respiration, and ATP production (Figures 7K and 7L). Boosting NAD(H) with NAM, NR, and NMN restored these mitochondrial respiratory parameters in *ATG5*$^{-/-}$ neurons to the levels in WT neurons (Figures 7K and 7L). These data suggest that restoration of $\Delta\Psi_m$ and mitochondrial bioenergetics underlies the cytoprotective effects of enhancing NAD(H) levels in *ATG5*$^{-/-}$ neurons. This is particularly important for differentiated cells like neurons, which have high energy demand and are greatly reliant on mitochondrial oxidative phosphorylation for energy production.[44]

Mitochondrial dysfunction perturbs proteostasis in autophagy-deficient neurons

Since autophagy is the primary clearance route for aggregated proteins, malfunction of this degradative process leads to proteotoxic stress during aging and neurodegenerative diseases.[10,11,45] Recent studies have demonstrated a crosstalk between mitochondrial and protein homeostasis, also involving NAD homeostasis, wherein NAD(H) boosters enhanced mitochondrial function and attenuated amyloid accumulation in aged worms and mice.[46–49] We therefore studied this phenomenon in autophagy-deficient human neurons using ProteoStat staining, which can detect aggresomes (inclusion bodies) of aggregated proteins.[50] As expected, *ATG5*$^{-/-}$ hESCs and hESC-derived NPs and neurons displayed a substantial increase in ProteoStat signal compared with the respective WT cell types (Figures 7M, 7N, and S7I–S7L), indicating accumulation of aggresomes in autophagy-deficient cells. Remarkably, increasing NAD(H) levels with NAM, NR, and NMN markedly reduced the ProteoStat signal in *ATG5*$^{-/-}$ cells (Figures 7M, 7N, and S7I–S7L), suggesting that NAD(H) boosters improved proteostasis, which is concomitant with restoring mitochondrial function (Figures 7I–7L). To further study this crosstalk, we used trehalose, a non-reducing disaccharide that prevents protein aggregation.[51] Trehalose reduced the ProteoStat signal and also restored $\Delta\Psi_m$ in *ATG5*$^{-/-}$ neurons (Figures 7M, 7N, and S7M), suggesting that suppression of aggresomes improved $\Delta\Psi_m$. Overall, our data show that NAD(H) boosters could improve cell survival by restoring mitochondrial and protein homeostasis during loss of autophagy.

DISCUSSION

In summary, we have established a human neuronal platform with autophagy deficiency by harnessing an hESC-based system. This human-relevant genetic model was used to study a fundamental question pertaining to how abrogation of autophagy compromises cell survival. We initially showed a causal link between loss of autophagy and cytotoxicity in human neurons, consistent with the genetic studies in mice,[5,6] implying that dysfunctional autophagy in neurodegenerative disease patients contributes to disease pathology.[10,11,13,14] Next, we investigated possible cellular mechanisms behind this phenomenon. *ATG5*$^{-/-}$ neurons were associated with metabolic defects underlying cell death at basal state. We found increased glucose uptake and greater use of glucose in glycolysis and TCA cycle in *ATG5*$^{-/-}$ neurons as an attempt to deal with their metabolic stress, but this was inadequate to restore the depleted metabolites in these metabolic networks. Our data suggest a specific

Figure 7. Boosting NAD(H) levels rescues mitochondrial function and proteostasis in *ATG5*$^{-/-}$ neurons

(A–E) Measurements of NAD^+ and NADH levels in cytoplasmic (cyto) and mitochondrial (mito) fractions (A), TMRE Δ fluorescence intensity (pre- and post-FCCP treatment) for ΔΨm (B) and H_2DCF-DA fluorescence intensity for ROS (C), immunofluorescence images of TUJ1 with MitoTracker staining (D), and analysis of average mitochondrial rod length per image (E) in *ATG5*$^{+/+}$ and *ATG5*$^{-/-}$ hESC-derived neurons (3 weeks).

(F–N) Measurements of NAD^+ and NADH levels (F); immunofluorescence images of TUJ1 with TUNEL staining (G); quantification of $TUNEL^+$ apoptotic nuclei (H); measurement of TMRE Δ fluorescence intensity (I and J); post-mitochondrial stress test measurement of basal respiration, maximal respiration, ATP production (K), and oxygen consumption rate (OCR) levels (L) after addition of oligomycin (Oligo), BAM15, and rotenone (Rot)/antimycin A (AA); fluorescence images of ProteoStat staining for aggresome detection (M); and quantification of ProteoStat fluorescence intensity in arbitrary units (a.u.) (N) in *ATG5*$^{+/+}$ and *ATG5*$^{-/-}$_5 hESC-derived neurons (3 weeks), where *ATG5*$^{-/-}$ neurons were treated with or without 1 μM CP2 (F–I), 1 mM NAM (I and K–N), 1 mM NR (J–N), 1 mM NMN (J–N), 1 mM L-Trp (J), or 100 mM trehalose (Tre) (M and N) for the last 6 days of neuronal differentiation period.

(O) Schematic representation of cell death cascade mediated by NAD(H) depletion in human neurons with loss of autophagy, and the cytoprotective effects of NAD(H) boosting agents.

Graphical data are mean ± SEM of n = 3–28 biological replicates as indicated. p values were calculated by one-way ANOVA followed by multiple comparisons with two-stage linear step-up procedure of Benjamini, Krieger, and Yekutieli (A–C, F, H–K, and N) or unpaired two-tailed Student's t test (E) on 3 independent experiments. ***$p < 0.001$; **$p < 0.01$; *$p < 0.05$; ns (non-significant). Scale bars: 10 μm (D), 20 μm (M), and 100 μm (G). MFI, mean fluorescent intensity.

See also Figure S7.

metabolic defect, attributed to NAD(H) depletion due to hyperactivation of NADases like PARPs and SIRTs and the consequent mitochondrial depolarization and bioenergetic deficit, as a potential mechanism leading to cell death due to autophagy deficiency (Figure 7O). These observations are supported by our results that boosting intracellular NAD(H) levels with bioavailable NAD precursors or other pharmacological agents improved mitochondrial function and cell viability in *ATG5*$^{-/-}$ neurons. Moreover, loss of autophagy is associated with increased DNA damage and ROS,[38,41] which in turn can activate PARPs and SIRTs to cause NAD(H) exhaustion in *ATG5*$^{-/-}$ neurons. Interestingly, NAD(H) boosters also reduced aggresomes that are accumulated in autophagy-deficient cells, thereby supporting an extensive crosstalk between mitochondrial and protein homeostasis as reported in recent studies.[46–49]

We found the phenomenon of NAD(H) depletion and increased cell death to be common in proliferating *ATG5*$^{-/-}$ hESCs and post-mitotic *ATG5*$^{-/-}$ human neurons. Importantly, our recent study further supports an evolutionarily conserved role of autophagy in maintaining NAD(H) levels where boosting NAD(H) improved the survival of yeast, mouse cells, and neurodegenerative patient-derived neurons with loss or malfunction of autophagy.[52] Additionally, it is plausible that other metabolic changes could also have detrimental effects,[2] such as nucleic acid recycling defect in autophagy-deficient tumor-derived cell lines,[23] and hyperactivation of the stress responsive transcription factor Nrf2 in autophagy-deficient mouse hepatocytes.[53] Despite the inability of maintaining the intracellular pools of building blocks and energy carriers due to loss of autophagy, complex metabolic alterations can also occur, such as metabolic reprogramming in cancer cells via constitutive activation of Nrf2,[54,55] which is induced by accumulation of p62 in autophagy-deficient cells.[53] Further studies are warranted to understand how these and other mechanisms integrate with the critical role of NAD(H) depletion during autophagy deficiency.

Aging and neurodegenerative diseases are associated with impaired autophagic activity, accumulation of misfolded protein aggregates, lower NAD^+ levels, and mitochondrial dysfunction,[10,31,34,45,56,57] whereas supplementation with NAD^+ precursors is beneficial in transgenic animal and patient-derived induced pluripotent stem cell (iPSC) models.[30,34,58] Moreover, enhancing NAD^+ synthesis improves mitochondrial function and reduces protein aggregation,[47,49] which we also observed in *ATG5*$^{-/-}$ neurons. Our data provide a mechanistic link between loss of autophagy, NAD(H) depletion, and cell death and explain how pharmacologically boosting NAD(H) levels can be cytoprotective in human neurons with autophagy deficiency by restoring mitochondrial function and proteostasis (Figure 7O). We further showed that this approach was cytoprotective in patient iPSC-derived neurons of Niemann-Pick type C1 (NPC1) disease,[52] a neurodegenerative lysosomal storage disorder associated with severe impairment in autophagy,[59,60] where NAD(H) was found to be depleted in accordance with our data arising from human genetic model of autophagy deficiency.[52] This intervention could have therapeutic relevance in a range of age-related, degenerative, or lysosomal storage diseases linked to autophagy dysfunction,[10–14] where autophagy induction strategy might not be effective if the functionality of lysosomes is compromised or due to the diverse nature of autophagy defects at multiple stages of the pathway.

Limitations of the study

In this study, the experiments were performed primarily in WT and *ATG5*$^{-/-}$ hESC-derived neurons, while certain key phenotypes were confirmed in hESCs and hESC-derived NPs. We demonstrated that loss of autophagy mediates cytotoxicity by depletion of NAD(H) levels. We found that activation of SIRTs and PARPs mediated NAD(H) depletion, as determined by using chemical inhibitors and measuring the enzyme activity of SIRT1, SIRT2, PARP1, and PARP2. However, it was not feasible to confirm the role of these NADases by genetic approaches. This is because gene knockdown in human neurons is technically challenging. Moreover, creating knockouts of the individual NADases in hESCs containing *ATG5* gene deletion and then differentiating the respective double-knockout clones into neurons will be extremely challenging. It is also unclear how this additional genetic manipulation will impact the genome-edited *ATG5*$^{-/-}$ hESCs, which are already in stress, exhibiting higher basal cytotoxicity. Future work should also analyze the role of other NADases in various human cell types differentiated from hESCs.

STAR★METHODS

Detailed methods are provided in the online version of this paper and include the following:

- KEY RESOURCES TABLE
- RESOURCE AVAILABILITY
  - Lead contact
  - Materials availability
  - Data and code availability
- EXPERIMENTAL MODEL AND SUBJECT DETAILS
  - Culture of human embryonic stem cells
  - Culture of primary human fibroblasts and inactivated mouse embryonic fibroblasts
- METHOD DETAILS
  - Design of TALEN and targeting vector for *ATG5* gene knockout
  - Gene targeting in hESCs
  - Differentiation of hESCs into neural precursors and neurons
  - Formulation and delivery of lipid nanoparticles with mRNA
  - Compound treatment and amino acid supplementation
  - Immunoblotting analysis
  - Immunofluorescence
  - Image acquisition of fixed cells
  - Electron microscopy
  - Image analysis of pluripotency markers
  - Gene expression analysis
  - TUNEL assay for apoptotic cells
  - Cytotoxicity assay
  - DAPI staining for apoptotic nuclear morphology
  - DNA damage analysis
  - Cell proliferation analysis

- Axonal length measurement in neurons
- Proteostat aggresome assay
- Measurement of SIRT1, SIRT2, PARP1 and PARP2 enzyme activity
- NAD^+ and NADH measurements
- ATP and ADP measurements
- Mitochondrial $\Delta\Psi_m$ and ROS measurements
- Mitochondrial respiration measurement
- MitoTracker staining and mitochondrial rod/branch length analysis
- Mitochondrial and cytosolic fractionation
- Analysis of glucose concentration in the medium
- Analysis of amino acid concentrations in the medium by GC–MS
- [U-$^{13}C_6$]-glucose tracer labeling and analysis of metabolites by GC–MS
- LC–MS-based metabolomics
- Metabolomics data analysis

● QUANTIFICATION AND STATISTICAL ANALYSIS

SUPPLEMENTAL INFORMATION

Supplemental information can be found online at https://doi.org/10.1016/j.celrep.2023.112372.

ACKNOWLEDGMENTS

We are grateful to R. Alagappan, A. Kaur, R. Banerjee, M. Dawlaty, Q. Gao, S. Vats, L.A. Oakey, V. Stanulovic, M. Hoogenkamp, and J. Frampton for technical assistance or providing reagents; N. Watson for electron microscopy; W. Salmon for imaging assistance; H. Salmonowicz for summary cartoon illustration; M. Coleman and S. Chakrabortee for manuscript feedback; IBR Technology Hub (at University of Birmingham; UoB), Birmingham Metabolic Tracer Analysis Core (MTAC), and Keck Microscopy Facility (at Whitehead Institute for Biomedical Research) for support and resources; ChromaDex for providing NR; and NMN Bio for providing NMN. S.S. and V.I.K. are also former fellows for life at Hughes Hall, University of Cambridge, UK. This study was mainly supported by a Wellcome Trust Seed Award (109626/Z/15/Z), Wellcome Trust ISSF (1516ISSFFEL10), a LifeArc Philanthropic Award (P2019-0004), and a Birmingham Fellowship to S.S., along with a UKIERI-DST grant (2016-17-0087) to S.S.; the FAPESP-Birmingham-Nottingham Strategic Collaboration Fund; the UoB Brazil Visiting Fellowship and Rutherford Fellowship to S.S. and T.R.R.; a BBSRC and UoB-funded MIBTP Studentship (BB/T00746X/1) to M.E.K. and S.S.; BBSRC grants (BB/R008167/2 and BB/M023389/1), a JSPS grant (18KK0242), and an MRC studentship (BH174490) to V.I.K.; grants from Emerald Foundation, St. Baldrick's Foundation, and LEO Foundation (L18015) to M.A.C. and R.J.; NIH grants (R37HD045022, R01-NS088538, and R01-MH104610) to R.J.; NIH grants (RF1AG55549 and R01-NS107265) to E.T.; FAPESP grant (2015/02041-1) to T.R.R.; funding from NIHR Surgical Reconstruction and Microbiology Research Centre in Birmingham to A.A.; fellowships from the Uehara Memorial Foundation, the International Medical Research Foundation, and JSPS (19J12969) to T.K.; a Wellcome Trust Senior Research Fellowship (217202/Z/19/Z) to E.-M.F.; a Cancer Research UK Career Development Fellowship (C53309/A19702) to O.D.K.M.; a CRUK grant (C42109/A24757) to D.A.T.; and an MRC grant (MR/P007732/1) to T.B.

AUTHOR CONTRIBUTIONS

C.S., E.S., and S.S. designed and performed the majority of the experiments; M.A.C., M.C., J.R., D.A., A.M.P., A.A., L.S., E.G.O., T.K., P.K.P., S.L.-R., M.E.K., K.J.K., A.H.-U., M.Z., L.F.S.E.S., J.T., S.Z., G.W.H., C.W., E.R.K., D.C., S.T., E.T., G.S., Y.B., G.G.L., J.G., D.A.G., E.-M.F., T.R.R., T.B., O.D.K.M., D.A.T., H.W., R.J., and V.I.K. performed experiments, provided tools or methodologies, and/or analyzed data; S.S., V.I.K., R.J., M.A.C., T.R.R., E.T., A.A., T.K., O.D.K.M., D.A.T., and T.B. acquired funding; S.S. and V.I.K. conceptualized and administered the project; S.S. prepared the figures; S.S. and V.I.K. wrote the manuscript, and all authors contributed to and/or approved the final version.

DECLARATION OF INTERESTS

R.J. is cofounder of Fate Therapeutics, Fulcrum Therapeutics, and Omega Therapeutics and advisor to Dewpoint Therapeutics. E.S. is founder of NMN Bio Ltd. V.I.K. is a scientific advisor for Longaevus Technologies.

INCLUSION AND DIVERSITY

We support inclusive, diverse, and equitable conduct of research.

Received: March 3, 2022
Revised: January 22, 2023
Accepted: March 23, 2023

REFERENCES

1. Boya, P., Reggiori, F., and Codogno, P. (2013). Emerging regulation and functions of autophagy. Nat. Cell Biol. *15*, 713–720. https://doi.org/10.1038/ncb2788.
2. Lahiri, V., Hawkins, W.D., and Klionsky, D.J. (2019). Watch what you (self-) eat: autophagic mechanisms that modulate metabolism. Cell Metab. *29*, 803–826. https://doi.org/10.1016/j.cmet.2019.03.003.
3. Rabinowitz, J.D., and White, E. (2010). Autophagy and metabolism. Science *330*, 1344–1348. https://doi.org/10.1126/science.1193497.
4. Stavoe, A.K.H., and Holzbaur, E.L.F. (2019). Autophagy in neurons. Annu. Rev. Cell Dev. Biol. *35*, 477–500. https://doi.org/10.1146/annurev-cellbio-100818-125242.
5. Hara, T., Nakamura, K., Matsui, M., Yamamoto, A., Nakahara, Y., Suzuki-Migishima, R., Yokoyama, M., Mishima, K., Saito, I., Okano, H., and Mizushima, N. (2006). Suppression of basal autophagy in neural cells causes neurodegenerative disease in mice. Nature *441*, 885–889. https://doi.org/10.1038/nature04724.
6. Komatsu, M., Waguri, S., Chiba, T., Murata, S., Iwata, J.i., Tanida, I., Ueno, T., Koike, M., Uchiyama, Y., Kominami, E., and Tanaka, K. (2006). Loss of autophagy in the central nervous system causes neurodegeneration in mice. Nature *441*, 880–884. https://doi.org/10.1038/nature04723.
7. Bjedov, I., Toivonen, J.M., Kerr, F., Slack, C., Jacobson, J., Foley, A., and Partridge, L. (2010). Mechanisms of life span extension by rapamycin in the fruit fly Drosophila melanogaster. Cell Metab. *11*, 35–46. https://doi.org/10.1016/j.cmet.2009.11.010.
8. Suzuki, S.W., Onodera, J., and Ohsumi, Y. (2011). Starvation induced cell death in autophagy-defective yeast mutants is caused by mitochondria dysfunction. PLoS One *6*, e17412. https://doi.org/10.1371/journal.pone.0017412.
9. Levine, B., and Kroemer, G. (2008). Autophagy in the pathogenesis of disease. Cell *132*, 27–42. https://doi.org/10.1016/j.cell.2007.12.018.
10. Menzies, F.M., Fleming, A., Caricasole, A., Bento, C.F., Andrews, S.P., Ashkenazi, A., Füllgrabe, J., Jackson, A., Jimenez Sanchez, M., Karabiyik, C., et al. (2017). Autophagy and neurodegeneration: pathogenic mechanisms and therapeutic opportunities. Neuron *93*, 1015–1034. https://doi.org/10.1016/j.neuron.2017.01.022.
11. Nixon, R.A. (2013). The role of autophagy in neurodegenerative disease. Nat. Med. *19*, 983–997. https://doi.org/10.1038/nm.3232.
12. Seranova, E., Connolly, K.J., Zatyka, M., Rosenstock, T.R., Barrett, T., Tuxworth, R.I., and Sarkar, S. (2017). Dysregulation of autophagy as a common mechanism in lysosomal storage diseases. Essays Biochem. *61*, 733–749. https://doi.org/10.1042/EBC20170055.

13. Seranova, E., Palhegyi, A.M., Verma, S., Dimova, S., Lasry, R., Naama, M., Sun, C., Barrett, T., Rosenstock, T.R., Kumar, D., et al. (2020). Human induced pluripotent stem cell models of neurodegenerative disorders for studying the biomedical implications of autophagy. J. Mol. Biol. *432*, 2754–2798. https://doi.org/10.1016/j.jmb.2020.01.024.

14. Sarkar, S. (2013). Regulation of autophagy by mTOR-dependent and mTOR-independent pathways: autophagy dysfunction in neurodegenerative diseases and therapeutic application of autophagy enhancers. Biochem. Soc. Trans. *41*, 1103–1130. https://doi.org/10.1042/BST20130134.

15. Avior, Y., Sagi, I., and Benvenisty, N. (2016). Pluripotent stem cells in disease modelling and drug discovery. Nat. Rev. Mol. Cell Biol. *17*, 170–182. https://doi.org/10.1038/nrm.2015.27.

16. Soldner, F., and Jaenisch, R. (2018). Stem cells, genome editing, and the path to translational medicine. Cell *175*, 615–632. https://doi.org/10.1016/j.cell.2018.09.010.

17. Kuma, A., Hatano, M., Matsui, M., Yamamoto, A., Nakaya, H., Yoshimori, T., Ohsumi, Y., Tokuhisa, T., and Mizushima, N. (2004). The role of autophagy during the early neonatal starvation period. Nature *432*, 1032–1036. https://doi.org/10.1038/nature03029.

18. Mizushima, N., Yoshimori, T., and Ohsumi, Y. (2011). The role of Atg proteins in autophagosome formation. Annu. Rev. Cell Dev. Biol. *27*, 107–132. https://doi.org/10.1146/annurev-cellbio-092910-154005.

19. Kauffman, K.J., Dorkin, J.R., Yang, J.H., Heartlein, M.W., DeRosa, F., Mir, F.F., Fenton, O.S., and Anderson, D.G. (2015). Optimization of lipid nanoparticle formulations for mRNA delivery in vivo with fractional factorial and definitive screening designs. Nano Lett. *15*, 7300–7306. https://doi.org/10.1021/acs.nanolett.5b02497.

20. Chambers, S.M., Fasano, C.A., Papapetrou, E.P., Tomishima, M., Sadelain, M., and Studer, L. (2009). Highly efficient neural conversion of human ES and iPS cells by dual inhibition of SMAD signaling. Nat. Biotechnol. *27*, 275–280. https://doi.org/10.1038/nbt.1529.

21. Tao, Y., and Zhang, S.C. (2016). Neural subtype specification from human pluripotent stem cells. Cell Stem Cell *19*, 573–586. https://doi.org/10.1016/j.stem.2016.10.015.

22. Altman, B.J., and Rathmell, J.C. (2012). Metabolic stress in autophagy and cell death pathways. Cold Spring Harb. Perspect. Biol. *4*, a008763. https://doi.org/10.1101/cshperspect.a008763.

23. Guo, J.Y., Teng, X., Laddha, S.V., Ma, S., Van Nostrand, S.C., Yang, Y., Khor, S., Chan, C.S., Rabinowitz, J.D., and White, E. (2016). Autophagy provides metabolic substrates to maintain energy charge and nucleotide pools in Ras-driven lung cancer cells. Genes Dev. *30*, 1704–1717. https://doi.org/10.1101/gad.283416.116.

24. Lunt, S.Y., and Vander Heiden, M.G. (2011). Aerobic glycolysis: meeting the metabolic requirements of cell proliferation. Annu. Rev. Cell Dev. Biol. *27*, 441–464. https://doi.org/10.1146/annurev-cellbio-092910-154237.

25. Fernie, A.R., Carrari, F., and Sweetlove, L.J. (2004). Respiratory metabolism: glycolysis, the TCA cycle and mitochondrial electron transport. Curr. Opin. Plant Biol. *7*, 254–261. https://doi.org/10.1016/j.pbi.2004.03.007.

26. Gu, W., Gaeta, X., Sahakyan, A., Chan, A.B., Hong, C.S., Kim, R., Braas, D., Plath, K., Lowry, W.E., and Christofk, H.R. (2016). Glycolytic metabolism plays a functional role in regulating human pluripotent stem cell state. Cell Stem Cell *19*, 476–490. https://doi.org/10.1016/j.stem.2016.08.008.

27. Morzorati, S.L., McBride, W.J., and Frederickson, R.C. (1981). Excitatory effect of L-aspartate and L-glutamate on Purkinje cells in rat cerebellum. Brain Res. Bull. *7*, 445–447. https://doi.org/10.1016/0361-9230(81)90045-9.

28. Modoux, M., Rolhion, N., Mani, S., and Sokol, H. (2021). Tryptophan metabolism as a pharmacological target. Trends Pharmacol. Sci. *42*, 60–73. https://doi.org/10.1016/j.tips.2020.11.006.

29. Hasmann, M., and Schemainda, I. (2003). FK866, a highly specific noncompetitive inhibitor of nicotinamide phosphoribosyltransferase, represents a novel mechanism for induction of tumor cell apoptosis. Cancer Res. *63*, 7436–7442.

30. Fang, E.F., Lautrup, S., Hou, Y., Demarest, T.G., Croteau, D.L., Mattson, M.P., and Bohr, V.A. (2017). NAD^+ in aging: molecular mechanisms and translational implications. Trends Mol. Med. *23*, 899–916. https://doi.org/10.1016/j.molmed.2017.08.001.

31. Lautrup, S., Sinclair, D.A., Mattson, M.P., and Fang, E.F. (2019). NAD^+ in brain aging and neurodegenerative disorders. Cell Metab. *30*, 630–655. https://doi.org/10.1016/j.cmet.2019.09.001.

32. Yoshino, J., Baur, J.A., and Imai, S.I. (2018). NAD^+ intermediates: the biology and therapeutic potential of NMN and NR. Cell Metab. *27*, 513–528. https://doi.org/10.1016/j.cmet.2017.11.002.

33. Reiten, O.K., Wilvang, M.A., Mitchell, S.J., Hu, Z., and Fang, E.F. (2021). Preclinical and clinical evidence of NAD^+ precursors in health, disease, and ageing. Mech. Ageing Dev. *199*, 111567. https://doi.org/10.1016/j.mad.2021.111567.

34. Verdin, E. (2015). NAD^+ in aging, metabolism, and neurodegeneration. Science *350*, 1208–1213. https://doi.org/10.1126/science.aac4854.

35. Katsyuba, E., Romani, M., Hofer, D., and Auwerx, J. (2020). NAD^+ homeostasis in health and disease. Nat. Metab. *2*, 9–31. https://doi.org/10.1038/s42255-019-0161-5.

36. Cantó, C., Sauve, A.A., and Bai, P. (2013). Crosstalk between poly(ADP-ribose) polymerase and sirtuin enzymes. Mol. Aspects Med. *34*, 1168–1201. https://doi.org/10.1016/j.mam.2013.01.004.

37. Luna, A., Aladjem, M.I., and Kohn, K.W. (2013). SIRT1/PARP1 crosstalk: connecting DNA damage and metabolism. Genome Integr. *4*, 6. https://doi.org/10.1186/2041-9414-4-6.

38. Hewitt, G., and Korolchuk, V.I. (2017). Repair, reuse, recycle: the expanding role of autophagy in genome maintenance. Trends Cell Biol. *27*, 340–351. https://doi.org/10.1016/j.tcb.2016.11.011.

39. Ying, W. (2008). NAD^+/NADH and $NADP^+$/NADPH in cellular functions and cell death: regulation and biological consequences. Antioxid. Redox Signal. *10*, 179–206. https://doi.org/10.1089/ars.2007.1672.

40. Martínez-Reyes, I., and Chandel, N.S. (2020). Mitochondrial TCA cycle metabolites control physiology and disease. Nat. Commun. *11*, 102. https://doi.org/10.1038/s41467-019-13668-3.

41. Sedlackova, L., and Korolchuk, V.I. (2020). The crosstalk of NAD, ROS and autophagy in cellular health and ageing. Biogerontology *21*, 381–397. https://doi.org/10.1007/s10522-020-09864-0.

42. Pickles, S., Vigié, P., and Youle, R.J. (2018). Mitophagy and quality control mechanisms in mitochondrial maintenance. Curr. Biol. *28*, R170–R185. https://doi.org/10.1016/j.cub.2018.01.004.

43. Zhang, L., Zhang, S., Maezawa, I., Trushin, S., Minhas, P., Pinto, M., Jin, L.W., Prasain, K., Nguyen, T.D.T., Yamazaki, Y., et al. (2015). Modulation of mitochondrial complex I activity averts cognitive decline in multiple animal models of familial Alzheimer's Disease. EBioMedicine *2*, 294–305. https://doi.org/10.1016/j.ebiom.2015.03.009.

44. Zheng, X., Boyer, L., Jin, M., Mertens, J., Kim, Y., Ma, L., Ma, L., Hamm, M., Gage, F.H., and Hunter, T. (2016). Metabolic reprogramming during neuronal differentiation from aerobic glycolysis to neuronal oxidative phosphorylation. Elife *5*, e13374. https://doi.org/10.7554/eLife.13374.

45. Aman, Y., Schmauck-Medina, T., Hansen, M., Morimoto, R.I., Simon, A.K., Bjedov, I., Palikaras, K., Simonsen, A., Johansen, T., Tavernarakis, N., et al. (2021). Autophagy in healthy aging and disease. Nat. Aging *1*, 634–650. https://doi.org/10.1038/s43587-021-00098-4.

46. Ruan, L., Wang, Y., Zhang, X., Tomaszewski, A., McNamara, J.T., and Li, R. (2020). Mitochondria-associated proteostasis. Annu. Rev. Biophys. *49*, 41–67. https://doi.org/10.1146/annurev-biophys-121219-081604.

47. Romani, M., Sorrentino, V., Oh, C.M., Li, H., de Lima, T.I., Zhang, H., Shong, M., and Auwerx, J. (2021). NAD^+ boosting reduces age-associated amyloidosis and restores mitochondrial homeostasis in muscle. Cell Rep. *34*, 108660. https://doi.org/10.1016/j.celrep.2020.108660.

48. Nowicka, U., Chroscicki, P., Stroobants, K., Sladowska, M., Turek, M., Uszczynska-Ratajczak, B., Kundra, R., Goral, T., Perni, M., Dobson, C.M., et al. (2021). Cytosolic aggregation of mitochondrial proteins

disrupts cellular homeostasis by stimulating the aggregation of other proteins. Elife *10*, e65484. https://doi.org/10.7554/eLife.65484.

49. Katsyuba, E., Mottis, A., Zietak, M., De Franco, F., van der Velpen, V., Gariani, K., Ryu, D., Cialabrini, L., Matilainen, O., Liscio, P., et al. (2018). De novo NAD^+ synthesis enhances mitochondrial function and improves health. Nature *563*, 354–359. https://doi.org/10.1038/s41586-018-0645-6.
50. Navarro, S., and Ventura, S. (2014). Fluorescent dye ProteoStat to detect and discriminate intracellular amyloid-like aggregates in Escherichia coli. Biotechnol. J. *9*, 1259–1266. https://doi.org/10.1002/biot.201400291.
51. Sirangelo, I., and Irace, G. (2010). Inhibition of aggregate formation as therapeutic target in protein misfolding diseases: effect of tetracycline and trehalose. Expert Opin. Ther. Targets *14*, 1311–1321. https://doi.org/10.1517/14728222.2010.531012.
52. Kataura, T., Sedlackova, L., Otten, E.G., Kumari, R., Shapira, D., Scialo, F., Stefanatos, R., Ishikawa, K.I., Kelly, G., Seranova, E., et al. (2022). Autophagy promotes cell survival by maintaining NAD levels. Dev. Cell *57*, 2584–2598.e11. https://doi.org/10.1016/j.devcel.2022.10.008.
53. Komatsu, M., Kurokawa, H., Waguri, S., Taguchi, K., Kobayashi, A., Ichimura, Y., Sou, Y.S., Ueno, I., Sakamoto, A., Tong, K.I., et al. (2010). The selective autophagy substrate p62 activates the stress responsive transcription factor Nrf2 through inactivation of Keap1. Nat. Cell Biol. *12*, 213–223. https://doi.org/10.1038/ncb2021.
54. Mitsuishi, Y., Taguchi, K., Kawatani, Y., Shibata, T., Nukiwa, T., Aburatani, H., Yamamoto, M., and Motohashi, H. (2012). Nrf2 redirects glucose and glutamine into anabolic pathways in metabolic reprogramming. Cancer Cell *22*, 66–79. https://doi.org/10.1016/j.ccr.2012.05.016.
55. Saito, T., Ichimura, Y., Taguchi, K., Suzuki, T., Mizushima, T., Takagi, K., Hirose, Y., Nagahashi, M., Iso, T., Fukutomi, T., et al. (2016). p62/Sqstm1 promotes malignancy of HCV-positive hepatocellular carcinoma through Nrf2-dependent metabolic reprogramming. Nat. Commun. *7*, 12030. https://doi.org/10.1038/ncomms12030.
56. Hansen, M., Rubinsztein, D.C., and Walker, D.W. (2018). Autophagy as a promoter of longevity: insights from model organisms. Nat. Rev. Mol. Cell Biol. *19*, 579–593. https://doi.org/10.1038/s41580-018-0033-y.
57. Lin, M.T., and Beal, M.F. (2006). Mitochondrial dysfunction and oxidative stress in neurodegenerative diseases. Nature *443*, 787–795. https://doi.org/10.1038/nature05292.
58. Schöndorf, D.C., Ivanyuk, D., Baden, P., Sanchez-Martinez, A., De Cicco, S., Yu, C., Giunta, I., Schwarz, L.K., Di Napoli, G., Panagiotakopoulou, V., et al. (2018). The NAD^+ precursor nicotinamide riboside rescues mitochondrial defects and neuronal loss in iPSC and fly models of Parkinson's disease. Cell Rep. *23*, 2976–2988. https://doi.org/10.1016/j.celrep.2018.05.009.
59. Maetzel, D., Sarkar, S., Wang, H., Abi-Mosleh, L., Xu, P., Cheng, A.W., Gao, Q., Mitalipova, M., and Jaenisch, R. (2014). Genetic and chemical correction of cholesterol accumulation and impaired autophagy in hepatic and neural cells derived from Niemann-Pick Type C patient-specific iPS cells. Stem Cell Rep. *2*, 866–880. https://doi.org/10.1016/j.stemcr.2014.03.014.
60. Sarkar, S., Carroll, B., Buganim, Y., Maetzel, D., Ng, A.H.M., Cassady, J.P., Cohen, M.A., Chakraborty, S., Wang, H., Spooner, E., et al. (2013). Impaired autophagy in the lipid-storage disorder Niemann-Pick type C1 disease. Cell Rep. *5*, 1302–1315. https://doi.org/10.1016/j.celrep.2013.10.042.
61. Love, K.T., Mahon, K.P., Levins, C.G., Whitehead, K.A., Querbes, W., Dorkin, J.R., Qin, J., Cantley, W., Qin, L.L., Racie, T., et al. (2010). Lipid-like materials for low-dose, in vivo gene silencing. Proc. Natl. Acad. Sci. USA *107*, 1864–1869. https://doi.org/10.1073/pnas.0910603106.
62. Lengner, C.J., Gimelbrant, A.A., Erwin, J.A., Cheng, A.W., Guenther, M.G., Welstead, G.G., Alagappan, R., Frampton, G.M., Xu, P., Muffat, J., et al. (2010). Derivation of pre-X inactivation human embryonic stem cells under physiological oxygen concentrations. Cell *141*, 872–883. https://doi.org/10.1016/j.cell.2010.04.010.
63. Hu, K., Zatyka, M., Astuti, D., Beer, N., Dias, R.P., Kulkarni, A., Ainsworth, J., Wright, B., Majander, A., Yu-Wai-Man, P., et al. (2022). WFS1 protein expression correlates with clinical progression of optic atrophy in patients with Wolfram syndrome. J. Med. Genet. *59*, 65–74. https://doi.org/10.1136/jmedgenet-2020-107257.
64. Xia, J., and Wishart, D.S. (2011). Web-based inference of biological patterns, functions and pathways from metabolomic data using MetaboAnalyst. Nat. Protoc. *6*, 743–760. https://doi.org/10.1038/nprot.2011.319.
65. Pluskal, T., Castillo, S., Villar-Briones, A., and Oresic, M. (2010). MZmine 2: modular framework for processing, visualizing, and analyzing mass spectrometry-based molecular profile data. BMC Bioinf. *11*, 395. https://doi.org/10.1186/1471-2105-11-395.
66. Chambers, M.C., Maclean, B., Burke, R., Amodei, D., Ruderman, D.L., Neumann, S., Gatto, L., Fischer, B., Pratt, B., Egertson, J., et al. (2012). A cross-platform toolkit for mass spectrometry and proteomics. Nat. Biotechnol. *30*, 918–920. https://doi.org/10.1038/nbt.2377.
67. Cermak, T., Doyle, E.L., Christian, M., Wang, L., Zhang, Y., Schmidt, C., Baller, J.A., Somia, N.V., Bogdanove, A.J., and Voytas, D.F. (2011). Efficient design and assembly of custom TALEN and other TAL effector-based constructs for DNA targeting. Nucleic Acids Res. *39*, e82. https://doi.org/10.1093/nar/gkr218.
68. Cohen, M.A., Itsykson, P., and Reubinoff, B.E. (2007). Neural differentiation of human ES cells. Curr protoc cell biol. Curr. Protoc. Cell Biol. *Chapter 23*, Unit 23 27. https://doi.org/10.1002/0471143030.cb2307s36.
69. Heyes, J., Palmer, L., Bremner, K., and MacLachlan, I. (2005). Cationic lipid saturation influences intracellular delivery of encapsulated nucleic acids. J. Control. Release *107*, 276–287. https://doi.org/10.1016/j.jconrel.2005.06.014.
70. Seranova, E., Ward, C., Chipara, M., Rosenstock, T.R., and Sarkar, S. (2019). In vitro screening platforms for identifying autophagy modulators in mammalian cells. Methods Mol. Biol. *1880*, 389–428. https://doi.org/10.1007/978-1-4939-8873-0_26.
71. Sun, C., Rosenstock, T.R., Cohen, M.A., and Sarkar, S. (2022). Autophagy dysfunction as a phenotypic readout in hiPSC-derived neuronal cell models of neurodegenerative diseases. Methods Mol. Biol. *2549*, 103–136. https://doi.org/10.1007/7651_2021_420.
72. Hummon, A.B., Lim, S.R., Difilippantonio, M.J., and Ried, T. (2007). Isolation and solubilization of proteins after TRIzol extraction of RNA and DNA from patient material following prolonged storage. Biotechniques *42*, 467–470, 472. https://doi.org/10.2144/000112401.
73. E Silva, L.F.S., Brito, M.D., Yuzawa, J.M.C., and Rosenstock, T.R. (2019). Mitochondrial dysfunction and changes in high-energy compounds in different cellular models associated to hypoxia: implication to schizophrenia. Sci. Rep. *9*, 18049. https://doi.org/10.1038/s41598-019-53605-4.
74. Rosenstock, T.R., Sun, C., Hughes, G.W., Winter, K., and Sarkar, S. (2022). Analysis of mitochondrial dysfunction by microplate reader in hiPSC-derived neuronal cell models of neurodegenerative disorders. Methods Mol. Biol. *2549*, 1–21. https://doi.org/10.1007/7651_2021_451.
75. Valente, A.J., Maddalena, L.A., Robb, E.L., Moradi, F., and Stuart, J.A. (2017). A simple ImageJ macro tool for analyzing mitochondrial network morphology in mammalian cell culture. Acta Histochem. *119*, 315–326. https://doi.org/10.1016/j.acthis.2017.03.001.
76. Bligh, E.G., and Dyer, W.J. (1959). A rapid method of total lipid extraction and purification. Can. J. Biochem. Physiol. *37*, 911–917. https://doi.org/10.1139/o59-099.
77. Maddocks, O.D.K., Labuschagne, C.F., Adams, P.D., and Vousden, K.H. (2016). Serine metabolism supports the methionine cycle and DNA/RNA methylation through de novo ATP synthesis in cancer cells. Mol. Cell *61*, 210–221. https://doi.org/10.1016/j.molcel.2015.12.014.

STAR★METHODS

KEY RESOURCES TABLE

REAGENT or RESOURCE	SOURCE	IDENTIFIER
Antibodies		
Acetylated lysine	Cell Signaling Technology	Cat# 9441; RRID: AB_331805
Actin	Sigma-Aldrich	Cat# A2066; RRID: AB_476693
ATG5	NanoTools	Cat# 0262-100/ATG5-7C6
53BP1	Abcam	Cat# ab36823; RRID: AB_722497
LC3B	Novus Biologicals	Cat# NB100-2220; RRID: AB_10003146
LC3B	NanoTools	Cat# 0231-100/LC3-5F10; RRID: AB_2722733
Cleaved caspase-3$^{(Asp175)}$	Cell Signaling Technology	Cat# 9661; RRID: AB_2341188
GAPDH	Sigma-Aldrich	Cat# G8795; RRID: AB_1078991
GFP	Clontech	Cat# 632375;RRID: AB_2756343
Goat anti-mouse IgG (H + L), Alexa Fluor 488	Invitrogen	Cat# A-11001; RRID: AB_2534069
Goat anti-mouse IgG (H + L), Alexa Fluor 594	Invitrogen	Cat# A-11005; RRID: AB_2534073
Goat anti-rabbit IgG (H + L), Alexa Fluor 488	Invitrogen	Cat# A-11008; RRID: AB_143165
Goat anti-rabbit IgG (H + L), Alexa Fluor 594	Invitrogen	Cat# A-11012; RRID: AB_2534079
Donkey anti-goat IgG (H + L), Alexa Fluor 488	Invitrogen	Cat# A-11055; RRID: AB_2534102
Goat anti-mouse IgG, H&L chain specific peroxidase conjugate	Calbiochem	Cat# 401253; RRID: AB_437779
Goat anti-rabbit IgG, H&L chain specific peroxidase conjugate	Calbiochem	Cat# 401393; RRID: AB_437797
Ki-67	Cell Signaling Technology	Cat# 9449; RRID: AB_2797703
MAP2	Invitrogen	Cat# PA5-17646; RRID: AB_11006358
NANOG	R&D Systems	Cat# AF1997; RRID: AB_355097
NESTIN	BioLegend	Cat# 656802; RRID: AB_2562474
OCT-3/4	R&D Systems	Cat# AF1759; RRID: AB_354975
p62	BD Biosciences	Cat# 610832; RRID: AB_398151
p70 S6 kinase	Cell Signaling Technology	Cat# 9202; RRID: AB_331676
PARP1	Santa Cruz Biotechnology	Cat# sc-8007; RRID: AB_628105
PARP2	Santa Cruz Biotechnology	Cat# sc-393310
PAX6	BioLegend	Cat# 901301; RRID: AB_2565003
Phospho-Histone H2A.X$^{(Ser139)}$	Millipore	Cat# 05-636; RRID: AB_2755003
Phospho-p70 S6 kinase$^{(Thr389)}$	Cell Signaling Technology	Cat# 9206; RRID: AB_2285392
Phospho-S6 ribosomal protein $^{(Ser235/236)}$	Cell Signaling Technology	Cat# 2211; RRID: AB_331679
Poly(ADP-ribose)	Enzo Life Sciences	Cat# ALX-804-220-R100; RRID: AB_2052275
Rabbit anti-goat IgG, H&L chain specific peroxidase conjugate	Calbiochem	Cat# 401515; RRID: AB_437816
S6 ribosomal protein	Cell Signaling Technology	Cat# 2217; RRID: AB_331355
SIRT1	Abcam	Cat# ab7343; RRID: AB_305867
SIRT2	Proteintech	Cat# 19655-1-AP; RRID: AB_2878592
SOX2	R&D Systems	Cat# AF2018; RRID: AB_355110
SSEA4	R&D Systems	Cat# MAB1435; RRID: AB_357704
Tom20	Santa Cruz Biotechnology	Cat# sc-17764; RRID: AB_628381
TRA-1-60	R&D Systems	Cat# MAB4770; RRID: AB_2119062
Tubulin	Sigma-Aldrich	Cat# T6793; RRID: AB_477585
TUJ1 (TUBB3)	BioLegend	Cat# 801201; RRID: AB_2313773

(*Continued on next page*)

Continued

REAGENT or RESOURCE	SOURCE	IDENTIFIER
Chemicals, peptides and recombinant proteins		
Antimycin A	Sigma-Aldrich	Cat# A8674
EGF	Gibco	Cat# PHG0313
bFGF	Invitrogen	Cat# RP-8627
β-mercaptoethanol	Sigma-Aldrich	Cat# M3148
B27 Supplement	Gibco	Cat# 12587-010
Carbonyl cyanide-p-trifluoromethoxyphenylhydrazone (FCCP)	Sigma-Aldrich	Cat# C2920
Cholesterol	Sigma-Aldrich	Cat# C8667
Collagenase type IV	Gibco	Cat# 17104019
CM-H_2DCFDA	Invitrogen	Cat# C6827
CP2	Zhang et al.[43] (provided by E. Trushina)	N/A
Customized DMEM/F-12 without D-Glucose and Phenol Red	Cell Culture Technologies	Cat# 12161503
C12-200 LNP	Love et al.[61] (provided by Alnylam Pharmaceuticals)	N/A
1,2-dimyristoyl-sn-glycero-3-phosphoethanolamine-N-[methoxy(polyethylene glycol)-2000]	Avanti Polar Lipids	Cat# 880150
1,2-dioleoyl-sn-glycero-3-phosphoethanolamine	Avanti Polar Lipids	Cat# 870296
DMEM	Gibco	Cat# 41966-029
DMEM/F12	Gibco	Cat# 11320-074
EDTA	Invitrogen	Cat# 15575-038
FBS	Gibco	Cat# A5256701
FK866	Sigma-Aldrich	Cat# F8557
Geltrex	Gibco	Cat# A1413302
GlutaMAX	Gibco	Cat# 35050061
HPLC Chloroform	Honeywell Research Chemicals	Cat# 15644530
HPLC Methanol	Sigma-Aldrich	Cat# 34860
HPLC Water	Sigma-Aldrich	Cat# 270733
KnockOut Serum Replacement	Gibco	Cat# 10828-028
Laminin	Sigma-Aldrich	Cat# L2020
L-Alanine	Sigma-Aldrich	Cat# A26802
L-Arginine	Sigma-Aldrich	Cat# A5006
L-Glutamic acid	Sigma-Aldrich	Cat# G5667
L-glutamine	Gibco	Cat# 25030-024
L-Glycine	Sigma-Aldrich	Cat# G7126
L-Histidine	Sigma-Aldrich	Cat# H8000
L-Leucine	Sigma-Aldrich	Cat# L8000
L-Lysine	Sigma-Aldrich	Cat# L5501
L-Methionine	Sigma-Aldrich	Cat# M5308
L-Phenylalanine	Sigma-Aldrich	Cat# W358512
L-Proline	Sigma-Aldrich	Cat# P0380
L-Serine	Sigma-Aldrich	Cat# S4500
L-Tryptophan	Sigma-Aldrich	Cat# T0254
Methoxyamine hydrochloride	Sigma-Aldrich	Cat# 226904
Mitomycin C	Sigma-Aldrich	Cat# M4287
MitoTracker Red CMXRos	Invitrogen	Cat# M7512

(*Continued on next page*)

Continued

REAGENT or RESOURCE	SOURCE	IDENTIFIER
MTBSTFA	Restek	Cat# 35610
Nicotinamide (NAM)	Sigma-Aldrich	Cat# N3376
Nicotinamide mononucleotide (NMN)	Provided by NMN Bio	Cat# NMN01-16676
Nicotinamide riboside (NR)	Provided by ChromaDex	N/A
Non-essential amino acids	Gibco	Cat# 11140-035
N2 supplement	Gibco	Cat# 17502-048
Olaparib	Cambridge Biosciences	Cat# CAY10621
Oligomycin	Sigma-Aldrich	Cat# 495455
Penicillin/streptomycin	Gibco	Cat# 15070063
Pentanedioic-d_6 Acid (D_6-Glutaric acid)	CDN Isotopes	Cat# D-5227
Poly-L-Ornithine	Sigma-Aldrich	Cat# P4957
ProLong Gold Antifade Mountant with DAPI	Invitrogen	Cat# P36931
Protein A agarose	Invitrogen	Cat# 15918-014
Puromycin	Gibco	Cat# A1113803
Recombinant Human Noggin	Peprotech	Cat# 120-10C
ROCK inhibitor Y-27632	Stemgent	Cat# 04-0012-02
Rotenone	Sigma-Aldrich	Cat# R8875
SB431542	Stemgent	Cat# 04-0010-10
Sirtinol	Cambridge Biosciences	Cat# CAY10523
StemFlex Basal Medium	Gibco	Cat# A3349401
StemFlex 10X Supplement	Gibco	Cat# A3349201
StemPro Accutase	Gibco	Cat# A1110501
Tetramethylrhodamine, Ethyl Ester, Perchlorate (TMRE)	Invitrogen	Cat# T669
Trehalose	Sigma-Aldrich	Cat# T9531
[U-13C^6]-Glucose tracer	Cambridge Isotope Laboratories	Cat# CLM-1396
Critical commercial assays		
ApoSENSOR ADP/ATP Ratio Bioluminescent Assay Kit	BioVision	Cat# K255-200
Bio-Rad Protein Assay Kit II	Bio-Rad	Cat# 5000002
CytoTox-Glo Cytotoxicity Assay Kit	Promega	Cat# G9290
CyQUANT Cell Proliferation Assay	Thermo Fisher Scientific	Cat# C7026
Click-iT Plus TUNEL Assay Kit	Invitrogen	Cat# C10617
HT Universal Colorimetric PARP Assay Kit	R&D Systems	Cat# 4677-096-K
Mitochondria Isolation Kit for Cultured Cells	ThermoFisher	Cat# 89874
NAD/NADH Quantitation Colorimetric Kit	BioVision	Cat# K337-100
PARP1/2 Activity Assay Kit	R&D Systems	Cat# 4677-096-K
PROTEOSTAT Aggresome Detection Kit	Enzo	Cat# ENZ-51035-K100
Quant-iT RiboGreen RNA Assay	Invitrogen	Cat# R11490
RNase-free DNase Set	Qiagen	Cat# 79254
Seahorse XF Cell Mito Stress Test Kit	Agilent	Cat# 103015-100
SIRT1 Activity Assay Kit	Abcam	Cat# ab156065
SIRT2 Activity Assay Kit	Abcam	Cat# ab156066
Deposited data		
LC–MS metabolomics data	This paper	MassIVE: MSV000091468; Table S1
Experimental models: Cell lines		
ATG5$^{+/+}$ (WIBR3) hESCs	Lengner et al.[62]	N/A
ATG5$^{+/-}$ (clone #1, #2) hESCs	This paper	N/A

(*Continued on next page*)

Continued

REAGENT or RESOURCE	SOURCE	IDENTIFIER
ATG5$^{-/-}$ (clones #1, #3, #4, #5, #6) hESCs	This paper	N/A
Human fibroblasts (line C1)	Hu et al.[63]	N/A
Inactivated mouse embryonic fibroblasts	Lengner et al.[62]	N/A
Oligonucleotides		
Primers for qPCR	This paper	Table S5
TALENs targeting *ATG5*	This paper	N/A
Recombinant DNA		
ATG5 targeting donor vectors	This paper	N/A
Software and algorithms		
GraphPad Prism v8.3.1	GraphPad Software	https://www.graphpad.com/; RRID: SCR_002798
ImageJ v1.41	NIH	https://imagej.net/ij/index.html; RRID: SCR_003070
Magellan F50	Tecan	https://lifesciences.tecan.com/software-magellan; N/A
MetaboAnalyst 4.0	Xia and Wishart[64]	https://www.metaboanalyst.ca/; RRID: SCR_015539
MZMine 2.10	Pluskal et al.[65]	http://mzmine.github.io/; RRID: SCR_012040
ProteoWizard	Chambers et al.[66]	https://proteowizard.sourceforge.io/; RRID: SCR_012056

RESOURCE AVAILABILITY

Lead contact

Further information and request for resources and reagents should be directed to and will be fulfilled by the lead contact, Sovan Sarkar (s.sarkar@bham.ac.uk).

Materials availability

Further information and request for resources and reagents listed in key resources table should be directed to the lead contact. The parental hESC line (WIBR3 hESC), originally generated and published by Rudolf Jaenisch lab at the Whitehead Institute for Biomedical Research, was used in this study by Sovan Sarkar lab at the University of Birmingham under material transfer agreements, UBMTA 15–0593 and 15–0595.

Data and code availability

- Original data are available from the lead contact upon request. LC–MS based metabolomics data from this work is available in Supplemental Information (Table S1), and the raw data is also available in the MassIVE repository (MassIVE: MSV000091468).
- This paper does not report original code.
- Any additional information required to reanalyze the data is available from the lead contact upon request.

EXPERIMENTAL MODEL AND SUBJECT DETAILS

Culture of human embryonic stem cells

WIBR3 human embryonic stem cells (hESCs; *ATG5*$^{+/+}$),[62] and *ATG5*$^{+/-}$ (clone #1) and *ATG5*$^{-/-}$ (clones #1, #3, #4, #5 and #6) hESC lines were cultured on a feeder layer or feeder-free. Briefly, hESCs were cultured on a feeder layer of inactivated mouse embryonic fibroblasts (MEFs) in hESC medium consisting of DMEM/F12 (Gibco), 15% fetal bovine serum (HyClone), 5% KnockOut Serum Replacement (Gibco), 1% penicillin/streptomycin (Gibco), 1% L-glutamine (Gibco), 1% non-essential amino acids (Gibco), 4 ng/mL human recombinant basic fibroblast growth factor (bFGF; R&D Systems) and 0.1 mM β-mercaptoethanol (Sigma-Aldrich). For experimentation, the hESCs were cultured feeder-free on Geltrex (Gibco) basement membrane matrix in StemFlex Basal Medium supplemented with StemFlex 10X Supplement (Gibco) and 1% penicillin/streptomycin (Gibco), or on Matrigel (Stem Cell Technologies) basement membrane matrix in mTeSR1 medium supplemented with mTeSR1 5X supplement (Stem Cell Technologies) and 1% penicillin/streptomycin (Gibco). The hESCs were maintained on feeders or feeder-free in a humidified incubator with 5% CO_2 and 5% O_2 at 37°C. For

starvation-induced autophagy, hESCs and hESC-derived neural precursors were cultured in Hank's Balanced Salt Solution (HBSS; Gibco) as indicated. See the key resources table for further information of the hESC lines, medium and reagents used in this study.

Culture of primary human fibroblasts and inactivated mouse embryonic fibroblasts

Primary fibroblasts from a 70-years-old healthy male individual, obtained from the European Collection of Cell Cultures and designated as control 1 (C1),[63] were cultured in Advanced DMEM medium, supplemented with 10% fetal bovine serum, 1% penicillin/streptomycin and 1% GlutaMAX (all from Gibco), in a humidified incubator with 5% CO_2 at 37°C. MEF feeder layer (for hESC culture) was prepared by inactivating the MEFs with mitomycin C (Sigma-Aldrich),[62] and then cultured in DMEM medium supplemented with 10% fetal bovine serum, 1% penicillin/streptomycin, 1% L-glutamine and 1% non-essential amino acids (all from Gibco) in a humidified incubator with 5% CO_2 at 37°C. See the key resources table for further information of cell lines, medium and reagents used in this study.

METHOD DETAILS

Design of TALEN and targeting vector for *ATG5* gene knockout

A pair of TALENs (transcription activator-like effector nucleases) targeting *ATG5* gene was designed and constructed as per the TALEN construct assembly guidelines.[67] The sequence recognized by *ATG5* TALEN F is GAAATGGTGAGTGAAT, and *ATG5* TALEN R binds to AGTATATACTTAATGCT, with a 15 bp spacer sequence between these two binding sites. Targeting donor vector was designed as PGK-Puro-pA or PGK-Neo-pA cassette flanked by ~700 bp homology arms lying upstream and downstream of *ATG5* exon 3.

Gene targeting in hESCs

The WIBR3 hESC line was cultured in 10 μM ROCK inhibitor Y-27632 (Stemgent) for 24 h prior to electroporation. Cell were harvested and resuspended in phosphate buffered saline (PBS), and then electroporated with 40 μg of donor plasmids together with 5 μg of each TALEN-encoding plasmid via Gene Pulser Xcell System (Bio-Rad) at 250 V and 500 μF in 0.4 cm cuvettes. Cells were then plated on DR4 MEF feeders in hESC medium supplemented with ROCK inhibitor. Individual colonies were picked and expanded after 0.5 μg/mL puromycin (Gibco) or 400 μg/mL G418 selection (Gibco) for 10 to 14 days following electroporation. The correctly targeted clones were confirmed by Southern blot (NdeI digested) and Sanger sequencing.

Differentiation of hESCs into neural precursors and neurons

Differentiation of hESCs into neural precursor cells (NPs) and terminally differentiated human neurons were performed via the 'dual SMAD inhibition' method.[20] The hESC colonies were collected using 1.5 mg/mL collagenase type IV (Thermo Fisher Scientific), separated from the MEF feeder cells by gravity, and cultured in non-adherent suspension culture dishes (Corning) in NP medium (NPM) comprising DMEM/F12 supplemented with 2% B27, 1% penicillin/streptomycin, 1% L-glutamine and 1% non-essential amino acids (all from Gibco) supplemented with 500 ng/mL human recombinant Noggin (Peprotech) and 10 μM SB431542 (Stemgent) for the first 4 days. NPM supplemented with 500 ng/mL Noggin and 20 ng/mL bFGF (Invitrogen) was used sequentially in the next 2 days (days 6–7), and NPM supplemented with only 20 ng/mL bFGF were used sequentially in the following 7 days (days 7–14) for further NP differentiation. At day 14, NPs clusters were dissociated and plated onto 100 μg/mL poly-L-ornithine (Sigma-Aldrich) and 14 μg/mL laminin (Sigma-Aldrich) pre-coated culture dishes in N2–B27 medium comprising DMEM/F12 supplemented with 1% N2, 2% B27, 1% penicillin/streptomycin, 1% L-glutamine and 1% non-essential amino acids (all from Gibco) supplemented with 20 ng/mL bFGF and 20 ng/mL EGF (Gibco). After 7 days in culture, neural rosette-bearing cultures were dissociated using StemPro Accutase (Thermo Fisher Scientific) and subsequently expanded on poly-L-ornithine and laminin coated cell culture dishes at the density of ~1.5×10^6 cells per well (of 6-well plate) in N2–B27 medium supplemented with 20 ng/mL bFGF and 20 ng/mL EGF. The NPs derived from hESCs via the dual SMAD inhibition method carry an anterior identity, and commit to forebrain fates when cultured in the presence of bFGF and EGF.[21] Proliferating NPs were passaged up to 4 times before induction of terminal differentiation into neurons by growth factor withdrawal in N2–B27 medium.[59,68] Differentiated neurons were used for analysis 3–4 weeks after differentiation. See the key resources table for further information of the medium and reagents used for generation of NPs and neuronal differentiation.

Formulation and delivery of lipid nanoparticles with mRNA

C12-200 (courtesy of Alnylam Pharmaceuticals) was prepared[61] and mixed together with 1,2-dioleoyl-*sn*-glycero-3-phosphoethanolamine (DOPE; Avanti Polar Lipids), cholesterol (Sigma) and 1,2-dimyristoyl-*sn*-glycero-3-phosphoethanolamine-N-[methoxy(polyethylene glycol)-2000] (ammonium salt) (PEG; Avanti) at a 50:20:20:10 weight ratio in ethanol. Then, an aqueous phase containing human *ATG5* or *GFP* mRNA (TriLink Biotechnologies) in 10 mM citrate buffer was prepared. Syringe pumps were used to mix the ethanol and aqueous phases at a 1:3 ratio to generate C12-200 lipid nanoparticles (LNPs),[19] which were then dialyzed against 1x PBS in a 20k MWCO cassette at 4°C for 2 h. mRNA concentration was quantified using a modified Quant-iT RiboGreen RNA Assay (Invitrogen).[69] Cells (hESCs and hESC-derived neurons) were treated with 2 μg/mL C12-200 LNP containing human *ATG5* or *GFP* mRNA for 4 days with replenishment on day 2, or as indicated. See the key resources table for further information of the LNPs used in this study.

Compound treatment and amino acid supplementation

Compounds used for modulating cellular NAD(H) levels (Table S2): 1 mM Nicotinamide (NAM) (Sigma-Aldrich), 1 mM Nicotinamide riboside (NR) (ChromaDex), 1 mM Nicotinamide mononucleotide (NMN) (NMN Bio), 10 nM FK866 (Sigma-Aldrich), 20 μM Sirtinol (Cambridge Bioscience), 10 μM Olaparib (Cambridge Bioscience), 1 mM L-Tryptophan (Sigma-Aldrich) and 1 μM CP2 (from E. Trushina). Other treatments include 100 mM trehalose, and amino acid supplementations with 1 mM of L-Alanine, L-Arginine, L-Glutamic acid, L-Glycine, L-Histidine, L-Leucine, L-Lysine, L-Methionine, L-Phenylalanine, L-Proline and L-Serine (all from Sigma-Aldrich). Compound treatment was done in hESCs and hESC-derived NPs for 2 days (with replenishment on day 1), and in hESC-derived neurons for the last 6 days (with replenishment on day 3) of the 3 weeks neuronal differentiation period, or as indicated. See the key resources table for further information of the compounds and amino acids used in this study.

Immunoblotting analysis

Cell lysates of hESCs and hESC-derived NPs and neurons were subjected to immunoblot analysis as per established methodology.[60,70,71] Cell pellets were lysed on ice in 2X Lysis Buffer comprising 20 mM Tris-HCl pH 6.8, 137 mM NaCl, 1 mM EGTA, 1% Triton X-100, 10% glycerol and 25X Protease Inhibitor Cocktail (all from Sigma-Aldrich) (buffer made to 1X) for 30 min, boiled for 5–10 min at 100°C. Protein concentration of the lysates was measured by Bio-Rad Protein Assay (Bio-Rad), and equal amounts of protein (10–40 μg) per sample were subjected to SDS–PAGE and immunoblot analysis.[70,71] The blots were then incubated in Blocking Buffer (6% non-fat milk powder in PBS-Tween 20) for 1 h at room temperature. For cleaved caspase-3 immunoblotting, cells were lysed with RIPA Lysis Buffer comprising 50 mM Tris-HCl pH 8.0, 150 mM NaCl, 1 mM EDTA, 0.5% deoxycholate, 1% IGEPAL (all from Sigma-Aldrich), 0.1% SDS (Bio-Rad) and Complete Protease Inhibitor Cocktail (Roche), sonicated and centrifuged at 14000 rpm for 30 min at 4°C. The samples were subjected to SDS–PAGE on a 16.5% gel, followed by wet transfer on nitrocellulose membrane, then membrane was blocked in 1% glutaraldehyde solution (VWR Life Science) in TBS for 30 min and in Blocking Buffer for 1 h at room temperature. All the blots were incubated overnight in primary antibodies (see Table S3 for the list and dilutions of primary antibodies and the cell types used upon) at 4°C on an orbital shaker. The immunoblots were then probed with appropriate secondary antibodies (see Table S3 for the list and dilutions of secondary antibodies) conjugated to horseradish peroxidase (HRP) for 1 h at room temperature on an orbital shaker. The chemiluminescent signal was visualized using Amersham ECL or ECL Prime Western Blotting Detection Reagent and Amersham Hyperfilm ECL (GE Healthcare) via ECOMAX X-ray Film Processor (PROTEC). Densitometry analyses of immunoblots were done using ImageJ v1.48 (NIH) software. The data was expressed as a percentage of the control condition.[59,60,70,71] See the key resources table for further information of the primary and secondary antibodies used for immunoblotting analysis.

Immunofluorescence

Immunofluorescence analysis was performed in hESCs and hESC-derived NPs and neurons as per established methodology.[60,70,71] Cells were washed in PBS, fixed with 4% formaldehyde (Thermo Fisher Scientific) at room temperature for 15 min, permeabilised with 0.5% Triton X-100 (Sigma-Aldrich) for 10 min (for all primary antibodies except LC3 antibody) or with pre-chilled methanol for 5 min (for LC3 antibody), and incubated with Blocking Buffer (5% goat or donkey serum (Sigma-Aldrich) in PBS with or without 0.05% Tween 20 depending on the antibody specifications) for 1 h at room temperature. Cells were then incubated overnight with primary antibodies (see Table S4 for the list and dilutions of primary antibodies and the cell types used upon) at 4°C, followed by incubation with appropriate Alexa Fluor conjugated secondary antibodies (see Table S4 for the list and dilutions of secondary antibodies) for 1 h at room temperature. The coverslips were mounted on glass slides with ProLong Gold antifade reagent with DAPI (Invitrogen). See the key resources table for further information of the primary and secondary antibodies used for immunofluorescence analysis.

Image acquisition of fixed cells

Fluorescence images of fixed cells were acquired using EVOS FL Cell Imaging System (Thermo Fisher Scientific) with AMG 10x Plan FL and AMG 40x Plan FL lens, Leica DM6000 B (Leica Microsystems) with Leica DFC 350 FX R2 camera and with HC PL APO 40x/1.25 or HC PL APO 100x/1.40 oil immersion lens with Leica Application Suite X software (Leica Microsystems), or with PerkinElmer UltraView spinning disk confocal system (PerkinElmer) with an Orca-ER cooled–CCD camera (Hamamatsu) on a Zeiss Axiovert 200 (Carl Zeiss Inc.) with 63x 1.4NA plan-apochromat oil immersion lens using Volocity v6.1 software (Improvision).

Electron microscopy

Cells (hESCs) were fixed in 2.5% glutaraldehyde, 3% paraformaldehyde with 5% sucrose in 0.1 M sodium cacodylate buffer (pH 7.4) (Sigma-Aldrich), pelleted, and post-fixed in 1% OsO_4 in veronal-acetate buffer. The cell pellet was stained in block overnight with 0.5% uranyl acetate in veronal-acetate buffer (pH 6), then dehydrated and embedded in Embed-812 resin. Sections were cut on Reichert Ultracut-E microtome with a Diatome diamond knife at 50 nm thickness setting, stained with uranyl acetate and lead citrate, then examined using Tecnai Spirit TEM (FEI) at 80 kV and photographed with AMT CCD camera.[60]

Image analysis of pluripotency markers

Cells (hESCs) immunostained with antibodies for the respective pluripotency markers were imaged and analyzed for their fluorescence intensity relative to the hESC colony area using the ImageJ v1.41 software (NIH). The data was expressed relative to the control (*ATG5*$^{+/+}$) condition. Quantification was performed on ~25 colonies per sample.

Gene expression analysis

Total RNA from cells (hESCs and hESC-derived NPs and neurons) was extracted using Trizol (Ambion) followed by DNase treatment using the RNase-free DNase set (Qiagen).[72] Reverse transcription PCR (RT-PCR) was performed using M-MLV Reverse Transcriptase (Promega) and quantitative PCR (qPCR) was performed using the CFX Connect Real-Time System (Bio-Rad).[72] 25 μM of primers (primer sequences listed in Table S5) (Merck) were used in SYBR Green mastermix (Applied Biosystems) that was added to 5 ng of cDNA. Results were analyzed using $2^{-\Delta\Delta Ct}$ method and were normalised to the expression of the housekeeping gene *GAPDH*.

TUNEL assay for apoptotic cells

Cells (hESC-derived neurons) were stained with Click-iT Plus TUNEL Assay for *in situ* apoptosis detection, Alexa Fluor 488 dye (Invitrogen) (see key resources table), according to manufacturer's protocol. Cells were fixed with 4% formaldehyde (Thermo Fisher Scientific) for 15 min, permeabilised with 0.25% Triton X-100 (Sigma-Aldrich) for 20 min at room temperature and then washed with deionized water. Cells were incubated at 37°C for 10 min in TdT reaction buffer, followed by incubation with TdT reaction mixture containing TdT reaction buffer, EdUTP, TdT enzyme for 60 min at 37°C, washed with 3% BSA, and finally incubated with Click-iT Plus TUNEL reaction cocktail for 30 min at 37°C followed by washes with 3% BSA. For detection of TUNEL$^+$ apoptotic nuclei in neurons, cells were subjected to immunofluorescence by blocking with 3% BSA (in PBS) followed by incubation with TUJ1 antibody (in 3% BSA in PBS) overnight at 4°C, and thereafter incubated with Alexa Fluor 594 secondary antibody for 1 h at room temperature. Coverslips were mounted on glass slides with ProLong Gold antifade reagent with DAPI (Invitrogen). The quantification of TUNEL$^+$ apoptotic nuclei in TUJ1$^+$ neuronal cells was performed via fluorescence microscopy.[59] The percentage of TUNEL$^+$ nuclei was calculated from the total number of TUJ1$^+$ cells analyzed (~200–300 cells per sample were analyzed).

Cytotoxicity assay

Cytotoxicity was measured with CytoTox-Glo Cytotoxicity Assay (Promega) (see key resources table), according to manufacturer's protocol. This luminescence-based cytotoxicity assay measures the extracellular activity of a distinct dead-cell protease when it is released from membrane-compromised cells. Cells (hESCs and hESC-derived neurons) were incubated with CytoTox-Glo Assay Reagent (comprising Assay Buffer and AAF-Glo Substrate) for 15 min at room temperature in the dark, then luminescence was measured using EnSpire Multimode plate reader (PerkinElmer) and the readings obtained were attributed to the basal cytotoxicity per well (first reading). To estimate cell population per well, cells were further incubated with Lysis Reagent (comprising Assay Buffer and Digitonin) for 30 min at room temperature in the dark, after which luminescence was measured again (second reading). Cytotoxicity data were normalised by dividing the first reading (basal cytotoxicity per well) to the second reading (indicative of cell population per well) and expressed as a percentage.

DAPI staining for apoptotic nuclear morphology

For analyzing apoptotic nuclei morphology by DAPI staining in hESC-derived neurons immunostained with TUJ1 antibody (neuronal marker), the percentage of apoptotic nuclei was calculated from the total number of TUJ1$^+$ cells. Quantification was performed on ~150–200 cells per sample.

DNA damage analysis

Cells (hESC-derived neurons) were immunostained with phospho-Histone H2A.X$^{(Ser139)}$ or 53BP1 along with TUJ1 (neuronal marker), and the frequency of γH2AX or 53BP1 puncta (DNA damage markers) was assessed by ImageJ v1.41 (NIH). Quantification was performed on ~200 cells per condition.

Cell proliferation analysis

Cells (hESCs) immunostained with antibodies for Ki-67 (cell proliferation marker) and OCT4 (pluripotency marker) were imaged and assessed for the percentage of Ki-67$^+$ cells in OCT4$^+$ hESCs using the ImageJ v1.41 software (NIH). Quantification was performed on ~100 cells per sample.

Axonal length measurement in neurons

Cells (hESC-derived neurons) immunostained with TUJ1 antibody (neuronal marker) were imaged and analyzed for axonal length using the Analyze Skeleton plugin in the ImageJ v1.41 (NIH). Quantification was performed on ~5 images per sample and 1000–1500 lines per image.

Proteostat aggresome assay

Analysis of aggresomes, which are inclusion bodies of aggregated proteins, was performed in cells (hESCs and hESC-derived NPs and neurons) using ProteoStat Aggresome Detection Kit (Enzo) (see key resources table).[47,50] Cells were fixed with 4% formaldehyde (Thermo Fisher Scientific) for 15 min at room temperature and then permeabilised with 0.5% Triton X-100 (Sigma-Aldrich) for 1 h. After washing with DPBS, cells were stained with ProteoStat Aggresome Dye (1:2000 in 1X Assay Buffer) and Hoechst 33342 Nuclear Stain (1:1000 in 1X Assay Buffer) overnight at 4°C. Cells were washed with DPBS followed by mounting the cover slips onto glass slides with ProLong Gold antifade reagent (Invitrogen). Images were acquired using EVOS fluorescence microscope (Thermo Fisher

Scientific) with a Texas Red filter for ProteoStat dye and a DAPI filter for nuclear signal. Quantification of ProteoStat fluorescence intensity was done in ~150–200 cells per sample using ImageJ v1.41 software (NIH).

Measurement of SIRT1, SIRT2, PARP1 and PARP2 enzyme activity

Cells (hESC-derived neurons) were lysed with Lysis Buffer (20 mM Tris-HCl pH 7.4, 135 mM NaCl, 1.5 mM $MgCl_2$, 1 mM EGTA, 10% glycerol, 0.1% IGEPAL) followed by immunoprecipitation (IP) of SIRT1, SIRT2, PARP1 or PARP2 with the respective anti-SIRT1 (Abcam), anti-SIRT2 (Proteintech), anti-PARP1 or anti-PARP2 (Santa Cruz Biotechnology) antibody conjugated to Protein A Agarose beads (Invitrogen) (see Table S6 for the list and concentrations of primary antibodies). For each IP reaction, the agarose beads were washed with lysis buffer, then incubated with 6 μg of the primary antibody in lysis buffer for 4 h at 4 ºC, after which the beads–antibody complex was washed with lysis buffer and incubated with cell lysate (300 μg of total protein) overnight at 4 ºC. The immunoprecipitate was centrifuged and washed, then directly used for SIRT1 and SIRT2 activity assay using Fluorometric SIRT1 or SIRT2 Activity Assay Kit (Abcam), or for PARP1 and PARP2 activity assay using HT Universal Colorimetric PARP Assay Kit (R&D Systems), according to manufacturers' instructions. For SIRT1 and SIRT2 activity, measurement of fluorescence readout was performed for 30 min with 2 min interval to detect the saturating fluorescence reading by EnSpire Multimode microplate reader (PerkinElmer). For PARP1 and PARP2 activity, measurement of absorbance was done using Infinite F50 microplate reader and data was processed using Magellan F50 Software (Tecan). Data were obtained as relative fluorescence (for SIRTs) or absorbance (for PARPs) units, and expressed as fold change relative to the control condition. See the key resources table for further information of the primary antibodies used for immunoprecipitation and the reagents used for enzyme activity assays.

NAD^+ and NADH measurements

NAD^+ and NADH measurements were done using NAD/NADH Quantitation Colorimetric Kit (BioVision) (see key resources table), according to manufacturer's instructions. Cells (hESCs and hESC-derived neurons) were washed with cold PBS, then lysed with NADH/NAD Extraction Buffer and immediately freeze-thawed twice on dry ice, centrifuged at 14000 rpm for 5 min at 4°C. Half of the supernatant was incubated at 60°C for 30 min to decompose the NAD and detect the NADH. Both halves of the supernatants were then cooled on ice, transferred into a 96-well plate, followed by incubation in Reaction Mix comprising NAD Cycling Buffer and NAD Cycling Enzyme Mix for 5 min at room temperature. Then NADH Developer was added to each well and the reaction was left to cycle for 1–2 h at room temperature. Measurements of optical density (OD) at 450 nm using the EnSpire Multimode plate reader (PerkinElmer) were performed every 20-30 min to detect the saturating OD, then normalized to protein concentration via Bio-Rad Protein Assay (Bio-Rad) to measure pmol/μg of NAD^+ and NADH.

ATP and ADP measurements

Measurements of ATP and ADP were done using ApoSENSOR ADP/ATP Ratio Bioluminescent Assay Kit (BioVision) (see key resources table), as per manufacturer's instructions. A Reaction Mix containing Nucleotide Releasing Buffer (NRB) and ATP monitoring enzyme was added in the wells of a white-walled 96-well plate and kept at room temperature for a few hours to burn residual ATP levels. Cells (hESCs and hESC-derived neurons) cultured in another 96-well plate were incubated with NRB for 5 min at room temperature to release the ATP, and then the supernatant was transferred to appropriate wells of the white-walled 96-well plate. Luminescence was measured using EnSpire Multimode microplate reader (PerkinElmer) for determining ATP levels, and again measured after adding ADP Converting Enzyme for determining ADP levels. Data were normalised to protein concentration via Bio-Rad Protein Assay (Bio-Rad) and expressed as a percentage of the control condition.

Mitochondrial $\Delta\Psi_m$ and ROS measurements

Measurements of mitochondrial membrane potential ($\Delta\Psi_m$) and reactive oxygen species (ROS) were performed with TMRE (Invitrogen) and CM-H_2DCFDA (Invitrogen), respectively.[73,74] Briefly, cells (hESCs and hESC-derived neurons) were loaded with Microscopy Medium comprising 120 mM NaCl, 3.5 mM KCl, 0.4 mM KH_2PO_4, 5 mM $NaHCO_3$, 1.2 mM $NaSO_4$, 20 mM HEPES and 15 mM glucose in dH_2O adjusted to pH 7.4 and supplemented with 1 mM $CaCl_2$ (all from Sigma-Aldrich), and incubated with 500 nM TMRE (for $\Delta\Psi_m$ measurement) and 20 μM CM-H_2DCFDA (for ROS measurement) for 1 h at 37°C. The fluorescence signals of TMRE and CM-H_2DCFDA were acquired using EnSpire Multimode microplate reader (PerkinElmer) for a period of 5 min to get basal fluorescence, and again for TMRE for another 5 min after the addition of 10 μM FCCP (fluorocarbonyl cyanide phenylhydrazone). The baseline fluorescence was calculated as the mean of the last 5 fluorescence readings before the addition of FCCP (for TMRE and CM-H_2DCFDA), and the delta (Δ) fluorescence was calculated by subtracting the basal fluorescence from the average of first 5 fluorescence readings after FCCP treatment (for TMRE only).[73,74] Data were obtained as relative fluorescence units, normalised to protein concentration via Bio-Rad Protein Assay (Bio-Rad), and expressed as a percentage of the control condition. See the key resources table for further information of the reagents used for mitochondrial $\Delta\Psi_m$ and ROS measurements.

Mitochondrial respiration measurement

Cells (hESC-derived NPs) were seeded into an initial density of 8×10^4 cells per well in XF96 cell-culture microplates previously coated with PO-L. Neurons were generated from the NPs after differentiation for 4 weeks, amounting to ~6.5×10^4 cells per well in XF96 cell-culture microplates. Prior to the experiment, the original culture medium was replaced with Seahorse XF DMEM medium without

phenol red supplemented with 2.5 mM L-glutamine, 0.5 mM sodium pyruvate and 17.5 mM glucose (all from Agilent) (supplemented to match the levels of these components in the DMEM/F-12 medium in which the neurons were cultured), and the cells were incubated for 1 h in a non-CO_2 incubator. Preparation of all the regents was done while the cells were in the incubation period and following the manufacturer's instructions. Basal levels of oxygen consumption rates (OCR) were measured on an XFe96 Extracellular Flux Analyzer (Agilent). Cells were stimulated with 2 μM oligomycin, 3 μM BAM15 and 1 μM rotenone/antimycin A (all from Sigma-Aldrich), as per the instructions of XF Cell Mito Stress Test Kit (Agilent). A range of mitochondrial respiratory parameters were calculated, such as basal respiration, maximal respiration and ATP production, as per the equations below. CyQUANT Direct Cell proliferation assay (Thermo Fisher Scientific) was used to normalise cell number as per manufacturer's instructions. Fluorescence was measured in a FLUOstar Omega Plate Reader (BMG Labtech). See the key resources table for further information of the reagents used for mitochondrial respiration measurement.

Basal respiration = (measurement before oligomycin stimulation) – (rate measurement after rotenone/antimycin A stimulation);
Maximal respiration = (maximum rate measurement after BAM15 stimulation) – (minimum rate measurement after rotenone/antimycin A stimulation);
ATP production = (basal respiration) – (minimum rate measurement after oligomycin stimulation).

MitoTracker staining and mitochondrial rod/branch length analysis

MitoTracker Red CMXRos (Invitrogen) (see key resources table) was used to label mitochondria as per manufacturer's protocol. Cells (hESCs and hESC-derived neurons) were incubated with 100 nM MitoTracker Red CMXRos for 45 min at 37°C, after which the cells were either fixed and imaged for analysis or subjected to immunofluorescence with cell-specific markers. Mitochondrial rod/branch length analysis (after MitoTracker staining or Tom20 immunofluorescence) was done per cell in hESCs (~40 cells per sample and 5–50 fragments per cell were analyzed) and per field of view in neurons (~4 images per sample and 200–4000 fragments per image were analyzed) using the Analyze Skeleton plugin from the Mitochondrial Network Analysis (MiNA) toolset in ImageJ v1.41 (NIH).[75]

Mitochondrial and cytosolic fractionation

Mitochondrial and cytosolic fractions were prepared from cells (hESC-derived neurons) using Mitochondria Isolation Kit (Thermo Fisher Scientific) (see key resources table), according to the manufacturer's instructions. 2×10^7 cells were pelleted for each sample from which cytoplasmic and mitochondrial fractions were separated by centrifugation at 13,000 g at 4°C for 20 min, after which these subcellular fractions were immediately used for the measurements of NAD^+ and NADH.

Analysis of glucose concentration in the medium

Glucose concentrations in the medium of cells (hESC-derived neurons), and also in cell-free medium (blank), were measured using a Contour XT meter. Medium (10 μL) was applied to the test strip and a reading taken after a 5 s equilibration period. Data were normalised to the protein concentration of the samples (via Bio-Rad Protein Assay), and fold changes of different time-points (days 1, 2 and 3) were calculated relative to day 0. For cell-free medium, the concentration of glucose was shown at different time-points.

Analysis of amino acid concentrations in the medium by GC–MS

The medium of cells (hESC-derived neurons) and also in cell-free medium (blank) were collected for analysis of amino acid concentrations. Medium samples were extracted using a modified Bligh–Dyer procedure[76] where equal volumes of MeOH/H_2O/$CHCl_3$ (Sigma-Aldrich; Honeywell Research Chemicals) were used to partition small molecule metabolites into a biphasic solution. The upper polar layer was removed and dried down for gas chromatography-mass spectrometry (GC–MS) analysis. Dried extracts were derivatised using a two-step protocol. Samples are first treated with 2% methoxamine in pyridine (40 μL; 1 h at 60°C) (Sigma-Aldrich), followed by addition of MTBSTFA (50 μL; 1 h at 60°C) (Restek). Samples were centrifuged and the solution was transferred to glass vials for GC–MS analysis. GC–MS analysis was undertaken using an Agilent 7890B GC and 5977A MSD. 1 μL of sample was injected in splitless mode with helium carrier gas at a rate of 1 mL/min. Initial oven temperature was held at 100°C for 1 min before ramping to 180 °C at a rate of 20°C/min, followed by a ramp to 235 °C at a rate of 10°C/min, and a final ramp to 320 °C at a rate of 100°C/min with a 3 min hold. Compound detection was carried out in scan mode. Total ion count of each metabolite was normalised to the internal standard D_6-Glutaric acid (CDN Isotopes). Data were normalised to the protein concentration of the samples (via Bio-Rad Protein Assay), and fold changes of different time-points (days 1, 2 and 3) were calculated relative to day 0. For cell-free medium, the concentrations of metabolites were shown at different time-points. See the key resources table for further information of the reagents used for analysis of amino acid concentrations.

[U-$^{13}C_6$]-glucose tracer labeling and analysis of metabolites by GC–MS

After 3 weeks of neuronal differentiation as described in previous section, cells (hESC-derived neurons) were cultured in a customized DMEM/F-12 neuronal medium lacking D-Glucose and Phenol Red (Cell Culture Technologies), supplemented with [U-$^{13}C_6$]-Glucose tracer (Cambridge Isotope Laboratories), for 24 h. Cell and medium samples of hESC-derived neurons were extracted using a modified Bligh–Dyer procedure,[76] and samples were prepared for GC–MS analysis, as described above. Samples were analyzed using an Agilent 8890/5977B GC–MS. 1 μL of sample was injected in splitless mode with helium carrier gas at a rate of 1 mL/min.

Initial oven temperature was held at 100°C for 1 min before ramping to 170 °C at a rate of 10°C/min, followed by a ramp to 220 °C at a rate of 3°C/min and a final ramp to 300 °C at a rate of 10°C/min with a 5 min hold. Compound detection was carried out in scan mode. Total ion counts of each metabolite were normalised to the internal standard D6-Glutaric acid. The ^{13}C tracer data was corrected for natural abundance using in-house MATLAB scripts. Data were normalised to the protein concentration of the samples via Bio-Rad Protein Assay (Bio-Rad). See the key resources table for further information of the reagents used for analysis of [U-$^{13}C_6$]-Glucose tracer labeling.

LC–MS-based metabolomics

Liquid chromatography–mass spectrometry (LC–MS)-based metabolomics[77] was performed in hESC-derived neurons after 3 weeks of neuronal differentiation. Briefly, cells were washed with cold PBS and lysed on ice at 2×10^6 cells/mL concentration in Metabolite Extraction Buffer comprising 30% acetonitrile (Sigma-Aldrich), 50% methanol (Fisher Scientific) and 20% Milli-Q water. Samples were vortexed for 45 s, centrifuged at 13000 rpm for 5 min at 4°C, and the supernatants subjected to LC–MS using an Accela 600 LC system and Exactive mass spectrometer (Thermo Scientific). For separation of metabolites, a Sequant ZIC-pHILIC column (4.6 mm × 150 mm, 5 μm; Merck) was used with the mobile phase mixed by A = 20 mM ammonium carbonate in water and B = acetonitrile. A gradient program starting at 20% of A and linearly increasing to 80% at 30 min was used, followed by washing (92% of A for 5 min) and re-equilibration (20% of A for 10 min), and the total run time of the method was 45 min. The LC stream was desolvated and ionised in the HESI probe. The Exactive Mass Spectrometer was operated in full scan mode over a mass range of 70–1200 m/z at a resolution of 50000 with polarity switching. The LC–MS raw data was converted into mzML files via ProteoWizard and imported to MZMine 2.10 for peak extraction and sample alignment.[65,66] A house-made database integrating KEGG, HMDB and LIPID MAPS was used for the assignment of the LC–MS signals by searching the accurate mass, and the metabolites were confirmed by running their commercial standards. Peak areas of different metabolites were normalised to the total ionic count (TIC) minus blank, and were used for comparative quantification. See the key resources table for further information of the reagents and tools used for LC–MS-based metabolomics.

Metabolomics data analysis

Multivariate statistical analysis on MS-based metabolomics was performed using MetaboAnalyst 4.0.[64] Each of the metabolite peaks was first normalized by auto-scaling (mean-centred and divided by SD of each variable) and then principal component analysis (PCA) was applied. Metabolite fold change was calculated relative to *ATG5*$^{+/+}$ (wild-type) cells, and then converted to Log_2 values. Each metabolite was plotted on a heatmap, and all metabolites were also plotted on a heatmap with hierarchical clustering. Furthermore, a univariate statistical test coupled with fold change of each metabolite or each amino acid were plotted on volcano plots. The significance cut-off was set to an adjusted p value of 0.05 ($-Log_{10}$(*P*-adjusted) > 1.3) and a fold-change as indicated. Statistical significance was determined using the Student's *t*-test with p value corrected with Benjamini and Hochberg false discovery rate (FDR) method.

QUANTIFICATION AND STATISTICAL ANALYSIS

Quantification of data are described under various Methods sections where applicable. Graphical data are shown from $n = 3$ or more biological replicates from two or three independent experiments, as indicated in the figure legends. Graphical data are depicted by column graph scatter dot plot (mean ± s.e.m.) or violin plot (lines at median and quartiles) using GraphPad Prism v8.3.1 software (GraphPad). Statistical significance (p value) on all graphical data was determined by unpaired two-tailed Student's *t*-test with Welch correction or by one-way ANOVA followed by multiple comparisons with two-stage linear step-up procedure of Benjamini, Krieger and Yekutieli using GraphPad Prism v8.3.1 software (GraphPad). For metabolomics data analysis, statistical significance was determined by Student's *t*-test using Benjamini and Hochberg FDR method. ***p < 0.001; **p < 0.01; *p < 0.05; ns (non-significant).